

Electronic Supplementary Information for 'Addressing Molecular Optomechanical Effects in Nanocavity-Enhanced Raman Scattering beyond the Single Plasmonic Mode'

Yuan Zhang,^{*a} Ruben Esteban,^{*b,c} Roberto A. Boto,^b Mattin Urbieto,^b Xabier Arrieta,^c ChongXin Shan,^a Shuzhou Li,^d Jeremy J. Baumberg^e and Javier Aizpurua^{*b,c}

Contents

S1 Continuum-field Model of Molecular Optomechanics	S1
S1.1 Effective Master Equation	S1
S1.2 Expressions to Obtain the SERS Spectrum	S4
S1.3 Negligible Correlation of Vibrational Modes	S5
S2 Identification of the Dipolar Contribution in the Plasmonic Response	S6
S2.1 Calculation of the Fitting Parameters for the Local Electric Field and the Dyadic Green's Function within the Single-mode Model	S7
S3 Dyadic Green's Function of a Metal-Insulator-Metal Structure	S7
S4 Additional Numerical Results	S8
S4.1 Raman Tensor of Biphenyl-4-thiol Molecule	S8
S4.2 Identification of Plasmonic Modes based on the Near-field Maps	S9
S4.3 Optomechanical Parameters for the Intermediate-Frequency Vibrational Mode at 1269 cm ⁻¹	S10
S4.4 Evolution of the Integrated Stokes Intensity for the Low-Frequency Vibrational Mode at 1066 cm ⁻¹	S11
S4.5 Laser Threshold to Reach the Vibrational Pumping Regime	S11
S4.6 Laser Threshold to Reach the Parametric Instability and Saturation of the Vibrational Population	S12
S4.7 Comparison with the Classical SERS Theory	S13
S4.8 SERS Enhancement of the 1066 cm ⁻¹ Vibrational Mode	S13
S4.9 Optomechanical Parameters of the Molecule in Vacuum	S14

S1 Continuum-field Model of Molecular Optomechanics

In this section, we present the continuum-field model of molecular optomechanics which follows the approach introduced by M.

^a Henan Key Laboratory of Diamond Optoelectronic Materials and Devices, Key Laboratory of Material Physics, Ministry of Education, School of Physics and Microelectronics, Zhengzhou University, Zhengzhou 450052, China; E-mail: yzhuaudipc@zzu.edu.cn

^b Center for Material Physics (CSIC - UPV/EHU), Paseo Manuel de Lardizabal 5, Donostia-San Sebastian, Gipuzkoa 20018 Spain; E-mail: aizpurua@ehu.es

^c Donostia International Physics Center, Paseo Manuel de Lardizabal 4, Donostia-San Sebastian, 20018 Spain; E-mail: ruben_esteban@ehu.es

^d School of Materials Science and Engineering, Nanyang Technological University, Nanyang Avenue 50, 639798 Singapore;

^e NanoPhotonics Centre, Cavendish Laboratory, University of Cambridge, Cambridge CB3 0HE, United Kingdom

K. Dezfouli and S. Hughes.¹ We initially derive equations for an arbitrary number of vibrations in the molecule, and later show that these vibrations can be typically treated as independent. This section is divided into three subsections, which address separately the derivation of the effective master equation for the molecular vibrations, the formulas to compute the Raman spectrum, and the demonstration that the quantum correlations between different vibrational modes are typically small and can thus be ignored.

S1.1 Effective Master Equation

We consider off-resonant SERS and thus focus on the electronic ground state of the molecule. We assume a parabolic potential energy surface for this state and model molecular vibrations as quantized harmonic oscillators via the Hamiltonian $\hat{H}_m = \sum_v \hbar \omega_v \hat{b}_v^\dagger \hat{b}_v$, where ω_v , \hat{b}_v^\dagger and \hat{b}_v are the vibrational frequency and the creation and annihilation bosonic operators of the vibrations, respectively. The index v labels the different vibrational modes.

On the other hand, the plasmonic response of the metallic nanostructure can be described within the quantum theory of the electromagnetic fields in a dispersive and lossy medium²⁻⁴. In this description, the Hamiltonian $\hat{H}_f = \int d^3\mathbf{r} \int_0^\infty d\omega \hbar \omega \hat{\mathbf{f}}^\dagger(\mathbf{r}, \omega) \cdot \hat{\mathbf{f}}(\mathbf{r}, \omega)$ accounts for the continuum of electromagnetic fields of the cavity with frequency ω and creation $\hat{\mathbf{f}}^\dagger(\mathbf{r}, \omega)$ and annihilation $\hat{\mathbf{f}}(\mathbf{r}, \omega)$ (noise) bosonic operators at position \mathbf{r} . The quantized electric field operator is expressed as

$$\hat{\mathbf{E}}(\mathbf{r}, \omega) = i \frac{\omega^2}{c_0^2} \int d^3\mathbf{r}' \sqrt{\frac{\hbar \epsilon^l(\mathbf{r}', \omega)}{\pi \epsilon_0}} \overleftrightarrow{\mathbf{G}}(\mathbf{r}, \mathbf{r}'; \omega) \cdot \hat{\mathbf{f}}(\mathbf{r}', \omega), \quad (\text{S1})$$

determined by the imaginary part of the dielectric function $\epsilon^l(\mathbf{r}', \omega)$ and the dyadic Green's function, which is the solution of the Helmholtz equation

$$\left[\nabla \times \nabla \times - \frac{\omega^2}{c_0^2} \epsilon(\mathbf{r}, \omega) \right] \overleftrightarrow{\mathbf{G}}(\mathbf{r}, \mathbf{r}'; \omega) = \delta(\mathbf{r} - \mathbf{r}'), \quad (\text{S2})$$

with c_0 speed of light and ϵ_0 vacuum dielectric permittivity.

The molecule couples to the quantized electric field via the interaction Hamiltonian^{1,5} $\hat{H}_{int} = -\frac{1}{2} \hat{\mathbf{p}} \cdot \hat{\mathbf{E}}(\mathbf{r}_m)$, where $\hat{\mathbf{E}}(\mathbf{r}_m) = \int_0^\infty d\omega [\hat{\mathbf{E}}(\mathbf{r}_m, \omega) + \hat{\mathbf{E}}^\dagger(\mathbf{r}_m, \omega)]$ is the electric field at the molecular position \mathbf{r}_m , and the induced dipole operator $\hat{\mathbf{p}} = \overleftrightarrow{\alpha} \hat{\mathbf{E}}(\mathbf{r}_m)$ is given by the electric field $\hat{\mathbf{E}}(\mathbf{r}_m)$ and the polarizability tensor $\overleftrightarrow{\alpha}$. We can then expand $\overleftrightarrow{\alpha}$ with respect to the normal-mode coordinates of the molecular vibrational modes ν and focus on the first-order term $\sum_\nu \overleftrightarrow{\alpha}_\nu (\hat{b}_\nu + \hat{b}_\nu^\dagger)$, where the Raman polarizability tensor $\overleftrightarrow{\alpha}_\nu = Q_\nu^0 \overleftrightarrow{\mathbf{R}}_\nu$ is determined by the zero-point amplitude $Q_\nu^0 = \sqrt{\hbar/(2\omega_\nu)}$ and the Raman tensor $\overleftrightarrow{\mathbf{R}}_\nu$ of the molecular vibration ν . The zero-order term in the expansion of $\overleftrightarrow{\alpha}$ is independent of the molecular vibrations and is ignored here because it leads to elastic scattering instead of inelastic Raman scattering as considered in this work. Finally, we approximate the interaction Hamiltonian as $\hat{H}_{int} \approx -\frac{1}{2} \hat{\mathbf{p}} \cdot \hat{\mathbf{E}}(\mathbf{r}_m)$ with the induced Raman dipole $\hat{\mathbf{p}} \approx \sum_\nu \overleftrightarrow{\alpha}_\nu \hat{\mathbf{E}}(\mathbf{r}_m) (\hat{b}_\nu + \hat{b}_\nu^\dagger)$.

To proceed, it is convenient to follow Ref. 1 and treat the laser illumination as a classical field. This approximation corresponds to substituting the field operator $\hat{\mathbf{E}}(\mathbf{r}_m)$ in the definition of the induced Raman dipole operator $\hat{\mathbf{p}}$ by the classical local field $\frac{1}{2} [\mathbf{E}(\mathbf{r}_m, \omega_l) e^{-i\omega_l t} + \mathbf{E}^*(\mathbf{r}_m, \omega_l) e^{i\omega_l t}]$ that excites the molecule. We can then express the induced Raman dipole operator as $\hat{\mathbf{p}}_R \approx \frac{1}{2} \sum_\nu (\mathbf{p}_\nu e^{-i\omega_l t} + \mathbf{p}_\nu^* e^{i\omega_l t}) (\hat{b}_\nu + \hat{b}_\nu^\dagger)$, with $\mathbf{p}_\nu = Q_\nu^0 \overleftrightarrow{\mathbf{R}}_\nu \mathbf{E}(\mathbf{r}_m, \omega_l)$ for a molecular vibration ν . $\mathbf{E}(\mathbf{r}_m, \omega_l)$ corresponds to the local electric field induced by the laser at the molecular position, taking into account the plasmonic enhancement. The optomechanical interaction Hamiltonian can thus be written as

$$\hat{H}_{int} \approx -\hat{\mathbf{p}}_R \cdot \hat{\mathbf{E}}(\mathbf{r}_m), \quad (\text{S3})$$

where the electric field operator, explicitly appearing in eqn. (S3), remains quantized (note that there is no 1/2 prefactor when writing the Hamiltonian in the classical-illumination approximation). We focus on the slowly varying terms (rotating wave approximation), and finally obtain the following linearized interaction Hamiltonian:

$$\begin{aligned} \hat{H}_{int} &\approx -i \frac{1}{2} \int_0^\infty d\omega \frac{\omega^2}{c_0^2} \int d^3\mathbf{r} \sqrt{\frac{\hbar \epsilon^l(\mathbf{r}, \omega)}{\pi \epsilon_0}} \\ &\left\{ \sum_\nu (\hat{b}_\nu + \hat{b}_\nu^\dagger) \cdot [\mathbf{p}_\nu^* \cdot \overleftrightarrow{\mathbf{G}}(\mathbf{r}_m, \mathbf{r}; \omega) \cdot \hat{\mathbf{f}}(\mathbf{r}, \omega) e^{i\omega_l t} \right. \\ &\left. - \mathbf{p}_\nu \cdot \overleftrightarrow{\mathbf{G}}^*(\mathbf{r}_m, \mathbf{r}; \omega) \cdot \hat{\mathbf{f}}^\dagger(\mathbf{r}, \omega) e^{-i\omega_l t}] \right\}, \quad (\text{S4}) \end{aligned}$$

In the next step, we go from the Schrödinger picture to the interaction picture by transforming the interaction Hamiltonian according to $\tilde{H}_{int}(t) = e^{(i/\hbar)(\hat{H}_m + \hat{H}_f)t} \hat{H}_{int} e^{-(i/\hbar)(\hat{H}_m + \hat{H}_f)t}$. After some algebra, we achieve the following expression

$$\begin{aligned} \tilde{H}_{int}(t) &\approx -i \frac{1}{2} \int_0^\infty d\omega \frac{\omega^2}{c_0^2} \int d^3\mathbf{r} \sqrt{\frac{\hbar \epsilon^l(\mathbf{r}, \omega)}{\pi \epsilon_0}} \\ &\left\{ \sum_\nu (\hat{b}_\nu e^{-i\omega_l t} + \hat{b}_\nu^\dagger e^{i\omega_l t}) [\mathbf{p}_\nu^* \cdot \overleftrightarrow{\mathbf{G}}(\mathbf{r}_m, \mathbf{r}; \omega) \cdot \hat{\mathbf{f}}(\mathbf{r}, \omega) e^{-i(\omega - \omega_l)t} \right. \\ &\left. - \mathbf{p}_\nu \cdot \overleftrightarrow{\mathbf{G}}^*(\mathbf{r}_m, \mathbf{r}; \omega) \cdot \hat{\mathbf{f}}^\dagger(\mathbf{r}, \omega) e^{i(\omega - \omega_l)t}] \right\}. \quad (\text{S5}) \end{aligned}$$

To clarify the notation used above, we can also write the products of the induced dipole vector and the dyadic Green's tensor explicitly as

$$\mathbf{p}_\nu^* \cdot \overleftrightarrow{\mathbf{G}}(\mathbf{r}_m, \mathbf{r}; \omega) \cdot \hat{\mathbf{f}}(\mathbf{r}, \omega) = \sum_{j,k} p_{\nu,k}^* G_{kj}(\mathbf{r}_m, \mathbf{r}; \omega) \hat{f}_j(\mathbf{r}, \omega), \quad (\text{S6})$$

$$\mathbf{p}_\nu \cdot \overleftrightarrow{\mathbf{G}}^*(\mathbf{r}_m, \mathbf{r}; \omega) \cdot \hat{\mathbf{f}}^\dagger(\mathbf{r}, \omega) = \sum_{j,k} p_{\nu,k} G_{kj}^*(\mathbf{r}_m, \mathbf{r}; \omega) \hat{f}_j^\dagger(\mathbf{r}, \omega), \quad (\text{S7})$$

in terms of the different components $p_{\nu,k}$, $G_{kj}(\mathbf{r}_m, \mathbf{r}; \omega)$, $\hat{f}_j(\mathbf{r}, \omega)$, $\hat{f}_j^\dagger(\mathbf{r}, \omega)$ in the Cartesian coordinate system ($j, k = x, y, z$).

We apply next the Born-Markovian approximation and obtain the standard master equation for open quantum system⁶

$$\frac{d}{dt} \tilde{\rho}(t) = -\frac{1}{\hbar^2} \int_0^\infty d\tau \text{tr}_R \left\{ [\tilde{H}_{int}(t), [\tilde{H}_{int}(t - \tau), \tilde{\rho}(t) \tilde{\rho}_R]] \right\}, \quad (\text{S8})$$

where $\tilde{\rho}$ and $\tilde{\rho}_R$ are the density operator of the molecular vibrations and the electromagnetic field reservoir, respectively, and tr_R is the trace over the reservoir. We also assume the following bath relations for the electromagnetic field operators¹

$$\text{tr}_R \left\{ \hat{f}_j(\mathbf{r}, \omega) \hat{f}_{j'}(\mathbf{r}', \omega') \tilde{\rho}_R \right\} = 0, \quad (\text{S9})$$

$$\text{tr}_R \left\{ \hat{f}_j^\dagger(\mathbf{r}, \omega) \hat{f}_{j'}^\dagger(\mathbf{r}', \omega') \tilde{\rho}_R \right\} = 0, \quad (\text{S10})$$

$$\text{tr}_R \left\{ \hat{f}_j^\dagger(\mathbf{r}, \omega) \hat{f}_{j'}(\mathbf{r}', \omega') \tilde{\rho}_R \right\} = 0, \quad (\text{S11})$$

$$\text{tr}_R \left\{ \hat{f}_j(\mathbf{r}, \omega) \hat{f}_{j'}^\dagger(\mathbf{r}', \omega') \tilde{\rho}_R \right\} = \delta_{jj'} \delta(\omega - \omega') \delta(\mathbf{r} - \mathbf{r}'). \quad (\text{S12})$$

By inserting eqn (S4) into eqn (S8), and using eqns (S9)-(S12), one obtains eqn (S13):

$$\begin{aligned}
\frac{\partial}{\partial t} \tilde{\rho}(t) = & -\frac{1}{4\hbar\pi\epsilon_0} \sum_{v,v'} \sum_k P_{v,k} \sum_{k'} P_{v',k'}^* \int_0^\infty d\omega \frac{\omega^2}{c_0^2} \frac{\omega'^2}{c_0^2} \int d\mathbf{r} \boldsymbol{\epsilon}^l(\mathbf{r}, \omega) \sum_j G_{kj}(\mathbf{r}_m, \mathbf{r}; \omega) G_{kj}^*(\mathbf{r}_m, \mathbf{r}; \omega) \\
& \times \int_0^\infty d\tau \left\{ e^{i(\omega - \omega_l + \omega_{v'})\tau} \left[\tilde{\rho}(t) \hat{b}_{v'} e^{-i\omega_{v'}\tau}, \hat{b}_v e^{-i\omega_l\tau} + \hat{b}_v^\dagger e^{i\omega_l\tau} \right] + e^{i(\omega - \omega_l - \omega_{v'})\tau} \left[\tilde{\rho}(t) \hat{b}_v^\dagger e^{i\omega_{v'}\tau}, \hat{b}_v e^{-i\omega_l\tau} + \hat{b}_v^\dagger e^{i\omega_l\tau} \right] \right\} \\
& - \frac{1}{4\hbar\pi\epsilon_0} \sum_{v,v'} \sum_k P_{v,k}^* \sum_{k'} P_{v',k'} \int_0^\infty d\omega \frac{\omega^2}{c_0^2} \frac{\omega'^2}{c_0^2} \int d\mathbf{r} \boldsymbol{\epsilon}^l(\mathbf{r}, \omega) \sum_j G_{kj}(\mathbf{r}_m, \mathbf{r}; \omega) G_{kj}^*(\mathbf{r}_m, \mathbf{r}; \omega) \\
& \times \int_0^\infty d\tau \left\{ e^{-i(\omega - \omega_l - \omega_{v'})\tau} \left[\hat{b}_v e^{-i\omega_l\tau} + \hat{b}_v^\dagger e^{i\omega_l\tau}, \hat{b}_{v'} e^{-i\omega_{v'}\tau} \tilde{\rho}(t) \right] + e^{-i(\omega - \omega_l + \omega_{v'})\tau} \left[\hat{b}_v e^{-i\omega_l\tau} + \hat{b}_v^\dagger e^{i\omega_l\tau}, \hat{b}_{v'}^\dagger e^{i\omega_{v'}\tau} \tilde{\rho}(t) \right] \right\}. \quad (S13)
\end{aligned}$$

Using the identity of the dyadic Green's function⁴

$$\begin{aligned}
& \left(\frac{\omega}{c_0} \right)^2 \sum_j \int d^3\mathbf{r}' \boldsymbol{\epsilon}^l(\mathbf{r}', \omega) G_{kj}(\mathbf{r}_1, \mathbf{r}'; \omega) G_{kj}^*(\mathbf{r}_2, \mathbf{r}'; \omega) \\
& = \text{Im} G_{k'k}(\mathbf{r}_1, \mathbf{r}_2; \omega), \quad (S14)
\end{aligned}$$

evaluating the time-integral with the relationship

$$\int_0^\infty d\tau e^{\mp i(\omega' - \omega)\tau} = \pi \delta(\omega' - \omega) \mp i \mathcal{P} \frac{1}{\omega' - \omega}, \quad (S15)$$

(with \mathcal{P} for the principal part), and applying the Kramer-Kronig relationship⁷

$$\mathcal{P} \int \frac{d\omega'}{\omega' - \omega} \frac{\omega'^2}{c_0^2} \text{Im} \overleftrightarrow{G}(\mathbf{r}, \mathbf{r}'; \omega') = \pi \frac{\omega^2}{c_0^2} \text{Re} \overleftrightarrow{G}(\mathbf{r}, \mathbf{r}'; \omega), \quad (S16)$$

we can rewrite eqn (S13) as

$$\begin{aligned}
\frac{\partial}{\partial t} \tilde{\rho}(t) = & -i \sum_{v,v'} S_{v'v}^-(\omega_l - \omega_{v'}) \left[\tilde{\rho}(t) \hat{b}_{v'} e^{-i\omega_{v'}t}, \hat{b}_v e^{-i\omega_l t} + \hat{b}_v^\dagger e^{i\omega_l t} \right] \\
& + i \sum_{v,v'} S_{v'v}^+(\omega_l - \omega_{v'}) \left[\hat{b}_v e^{-i\omega_{v'}t} + \hat{b}_v^\dagger e^{i\omega_{v'}t}, \hat{b}_v^\dagger e^{i\omega_l t} \tilde{\rho}(t) \right] \\
& - i \sum_{v,v'} S_{v'v}^-(\omega_l + \omega_{v'}) \left[\tilde{\rho}(t) \hat{b}_v^\dagger e^{i\omega_{v'}t}, \hat{b}_v e^{-i\omega_l t} + \hat{b}_v^\dagger e^{i\omega_l t} \right] \\
& + i \sum_{v,v'} S_{v'v}^+(\omega_l + \omega_{v'}) \left[\hat{b}_v e^{-i\omega_{v'}t} + \hat{b}_v^\dagger e^{i\omega_{v'}t}, \hat{b}_v e^{-i\omega_l t} \tilde{\rho}(t) \right], \quad (S17)
\end{aligned}$$

with the spectral densities defined as

$$S_{v'v}^+(\omega) = \frac{1}{4\hbar\epsilon_0} \left(\frac{\omega}{c_0} \right)^2 \mathbf{p}_{v'}^* \cdot \overleftrightarrow{G}(\mathbf{r}_m, \mathbf{r}_m; \omega) \cdot \mathbf{p}_v \quad (S18)$$

$$S_{v'v}^-(\omega) = \frac{1}{4\hbar\epsilon_0} \left(\frac{\omega}{c_0} \right)^2 \mathbf{p}_{v'}^* \cdot \overleftrightarrow{G}^*(\mathbf{r}_m, \mathbf{r}_m; \omega) \cdot \mathbf{p}_v. \quad (S19)$$

Here $\overleftrightarrow{G}(\mathbf{r}_m, \mathbf{r}_m; \omega)$ denotes the near-field dyadic Green's function, as in the main text. We have solved the master equation (S17) and verified that the off-resonant terms involving two creation or annihilation operators (e.g. $\hat{b}_v \hat{b}_v$) are usually several orders of magnitude smaller than the resonant terms involving one creation and one annihilation operator (e.g. $\hat{b}_v \hat{b}_v^\dagger$). Therefore, it is fully justified to ignore these off-resonant terms in eqn (S17) by applying the rotating wave approximation.

In the next step, we adopt the following abbreviations:

$$\Omega_{v'v}^\pm = S_{v'v}^+(\omega_l \mp \omega_{v'}) + S_{v'v}^-(\omega_l \mp \omega_{v'}), \quad (S20)$$

$$\Gamma_{v'v}^\pm = -i[S_{v'v}^+(\omega_l \mp \omega_{v'}) - S_{v'v}^-(\omega_l \mp \omega_{v'})]. \quad (S21)$$

By inserting eqn (S18-S19) into eqn (S20-S21) for $v' = v$, we obtain

$$\Omega_{vv}^\pm = \frac{1}{2\hbar\epsilon_0} \left(\frac{\omega_l \mp \omega_v}{c_0} \right)^2 \mathbf{p}_v^* \cdot \text{Re} \overleftrightarrow{G}(\mathbf{r}_m, \mathbf{r}_m, \omega_l \mp \omega_v) \cdot \mathbf{p}_v, \quad (S22)$$

$$\Gamma_{vv}^\pm = \frac{1}{2\hbar\epsilon_0} \left(\frac{\omega_l \mp \omega_v}{c_0} \right)^2 \mathbf{p}_v^* \cdot \text{Im} \overleftrightarrow{G}(\mathbf{r}_m, \mathbf{r}_m, \omega_l \mp \omega_v) \cdot \mathbf{p}_v, \quad (S23)$$

which correspond to eqn (2) and eqn (6) in the main text.

Using the relation $\hat{b}_v \hat{b}_v^\dagger = \hat{b}_v^\dagger \hat{b}_v + \delta_{v,v'}$, and eqns (S20) and (S21), we can rewrite eqn (S17) as

$$\begin{aligned}
\frac{\partial}{\partial t} \tilde{\rho}(t) = & i \sum_{v,v'} \frac{1}{2} (\Omega_{v'v}^+ + \Omega_{v'v}^-) \left[\hat{b}_v^\dagger e^{i\omega_{v'}t} \hat{b}_{v'} e^{-i\omega_{v'}t}, \tilde{\rho}(t) \right] \\
& - \sum_{v,v'} \frac{1}{2} \Gamma_{v'v}^+ \left(\left\{ \hat{b}_v e^{-i\omega_{v'}t} \hat{b}_v^\dagger e^{i\omega_{v'}t}, \tilde{\rho}(t) \right\} - 2 \hat{b}_v^\dagger e^{i\omega_{v'}t} \tilde{\rho}(t) \hat{b}_v e^{-i\omega_{v'}t} \right) \\
& - \sum_{v,v'} \frac{1}{2} \Gamma_{v'v}^- \left(\left\{ \hat{b}_v^\dagger e^{i\omega_{v'}t} \hat{b}_v e^{-i\omega_{v'}t}, \tilde{\rho}(t) \right\} - 2 \hat{b}_v e^{-i\omega_{v'}t} \tilde{\rho}(t) \hat{b}_v^\dagger e^{i\omega_{v'}t} \right). \quad (S24)
\end{aligned}$$

We note that there is a factor of 4 difference in the prefactor of the last two lines of eqn (S24) with respect to the equations in Ref. 1, because we have defined the classical fields as $\frac{1}{2}[\mathbf{E}(\mathbf{r}_m, \omega_l) e^{-i\omega_l t} + \mathbf{E}^*(\mathbf{r}_m, \omega_l) e^{i\omega_l t}]$ (with the prefactor 1/2). Transforming eqn (S24) back to the Schrödinger picture and introducing the thermal pumping and the intrinsic decay rate γ_v of the molecular vibrations, we obtain the effective master equation for the reduced density operator $\hat{\rho}$ of the molecular vibrations:

$$\frac{\partial}{\partial t} \hat{\rho} = -\frac{i}{\hbar} [\hat{H}_m + \hat{H}_{opt}, \hat{\rho}] + \mathcal{D}_{th}[\hat{\rho}] + \mathcal{D}_{opt}[\hat{\rho}]. \quad (S25)$$

In this equation, the Lindblad term

$$\mathcal{D}_{th}[\hat{\rho}] = \sum_v \frac{\gamma_v}{2} \left\{ \left(n_v^{th} + 1 \right) \mathcal{D}[\hat{b}_v] \hat{\rho} + n_v^{th} \mathcal{D}[\hat{b}_v^\dagger] \hat{\rho} \right\} \quad (S26)$$

describes the intrinsic decay and thermal pumping of molecular vibrations, where $n_v^{th} = \left[e^{\hbar\omega_v/k_B T} - 1 \right]^{-1}$ is the thermal vibra-

tional population at temperature T (k_B is the Boltzmann constant). Here, \mathcal{D} is the Lindblad super-operator $\mathcal{D}[\hat{\rho}] = 2\hat{\rho}\hat{\delta}^\dagger - \hat{\delta}^\dagger\hat{\rho} - \hat{\rho}\hat{\delta}$ (for any operator $\hat{\delta}$). The Hamiltonian

$$\hat{H}_{opt} = -\sum_{v,v'} \frac{\hbar}{2} (\Omega_{vv'}^+ + \Omega_{v'v}^-) \hat{b}_v^\dagger \hat{b}_{v'} \quad (S27)$$

describes the plasmon-induced vibrational frequency shift $-\frac{\hbar}{2} (\Omega_{vv}^+ + \Omega_{vv}^-)$ (for $v = v'$) and the plasmon-mediated coherent interaction between the molecular vibrations $-\frac{\hbar}{2} (\Omega_{vv'}^+ + \Omega_{v'v}^-)$ (for $v' \neq v$). Last, the terms

$$\mathcal{D}_{opt}[\hat{\rho}] = \frac{1}{2} \sum_{v,v'} \left\{ \Gamma_{v'v}^- \mathcal{D}[\hat{b}_v, \hat{b}_{v'}^\dagger] \hat{\rho} + \Gamma_{vv'}^+ \mathcal{D}[\hat{b}_v^\dagger, \hat{b}_{v'}] \hat{\rho} \right\} \quad (S28)$$

describe the plasmon-induced vibrational damping Γ_{vv}^- and pumping Γ_{vv}^+ (for $v = v'$) and the dissipative coupling $\Gamma_{v'v}^-, \Gamma_{vv'}^+$ (for $v' \neq v$), where the super-operator is defined as $\mathcal{D}[\hat{\rho}] = 2\hat{\delta}\hat{\rho} - \hat{\rho}\hat{\delta} - \hat{\rho}\hat{\delta}^\dagger$ (for any operator $\hat{\delta}$ and $\hat{\rho}$).

To obtain the physical quantities of interest, we use eqn (S25) to evaluate $\frac{\partial}{\partial t} \langle \hat{\delta} \rangle (t) = \text{tr} \left\{ \frac{\partial}{\partial t} \hat{\rho}(t) \right\}$ and thus derive sets of equations for the expectation values $\langle \hat{\delta} \rangle = \text{tr} \{ \hat{\delta} \hat{\rho}(t) \}$ of different operators $\hat{\delta}$. Setting $\hat{\delta}$ first to the operators $\hat{b}_v^\dagger \hat{b}_v$ and $\hat{b}_v^\dagger \hat{b}_{v'}$, we obtain the equations for the population $\langle \hat{b}_v^\dagger \hat{b}_v \rangle$ and the correlation $\langle \hat{b}_v^\dagger \hat{b}_{v'} \rangle$ of different vibrational modes ($v \neq v'$):

$$\begin{aligned} \frac{\partial}{\partial t} \langle \hat{b}_v^\dagger \hat{b}_{v'} \rangle &= -\kappa_{vv'} \langle \hat{b}_v^\dagger \hat{b}_{v'} \rangle + \eta_{vv'} \\ &+ i \sum_{v''} \langle \hat{b}_v^\dagger \hat{b}_{v''} \rangle v_{vv''}^{(1)} - i \sum_{v''} v_{vv''}^{(2)} \langle \hat{b}_{v''}^\dagger \hat{b}_{v'} \rangle, \end{aligned} \quad (S29)$$

Here, we have used the abbreviations $\tilde{\omega}_v = \omega_v - i\frac{1}{2}\gamma_v$, $\kappa_{vv'} = i(\tilde{\omega}_v - \tilde{\omega}_{v'}^*)$, $\eta_{vv'} = \Gamma_{vv'}^+ + \delta_{vv'} n^h \gamma_v$, $v_{vv'}^{(1)} = \frac{1}{2} (\Omega_{vv'}^+ + \Omega_{v'v}^-) - i\frac{1}{2} (\Gamma_{v'v}^+ - \Gamma_{vv'}^-)$, $v_{vv'}^{(2)} = \frac{1}{2} (\Omega_{v'v}^+ + \Omega_{vv'}^-) + i\frac{1}{2} (\Gamma_{vv'}^+ - \Gamma_{v'v}^-)$. As shown in the main text, it is convenient to introduce the effective optomechanical damping rate

$$\Gamma_v^{opt} = \Gamma_{vv}^- - \Gamma_{vv}^+, \quad (S30)$$

when we consider the vibrational population with eqn (S29) for $v = v'$. In a similar manner, setting $\hat{\delta}$ to \hat{b}_v and \hat{b}_v^\dagger , we derive the equations for the vibrational amplitudes $\langle \hat{b}_v \rangle$ and $\langle \hat{b}_v^\dagger \rangle$:

$$\frac{\partial}{\partial t} \langle \hat{b}_v \rangle = -i\tilde{\omega}_v \langle \hat{b}_v \rangle + i \sum_{v'} \langle \hat{b}_{v'} \rangle v_{vv'}^{(1)}, \quad (S31)$$

$$\frac{\partial}{\partial t} \langle \hat{b}_v^\dagger \rangle = i\tilde{\omega}_v^* \langle \hat{b}_v^\dagger \rangle - i \sum_{v'} v_{vv'}^{(2)} \langle \hat{b}_{v'}^\dagger \rangle, \quad (S32)$$

which will be used later to determine the SERS spectrum.

To solve the system of equations (S29) efficiently, we first express it in matrix form $\partial x/\partial t = -\left[\Gamma - i(V^{(1)} - V^{(2)}) \right] x + \lambda$, where x, λ are vectors and $\Gamma, V^{(1)}, V^{(2)}$ are matrices with elements $x_\alpha = \langle \hat{b}_v^\dagger \hat{b}_{v'} \rangle$, $\lambda_\alpha = \eta_{vv'}$, $\Gamma_{\alpha\beta} = \delta_{\alpha\beta} \kappa_{vv'}$, $V_{\alpha\beta}^{(1)} = \delta_{v,v''} v_{vv''}^{(1)}$, $V_{\alpha\beta}^{(2)} = \delta_{v',v''} v_{vv''}^{(2)}$. Here, we have defined the labels $\alpha = v \times n + v'$, $\beta = v'' \times n + v'''$ with n the total number of the vibrational modes. With the direct matrix inversion $x_{ss} = \left[\Gamma - i(V^{(1)} - V^{(2)}) \right]^{-1} \lambda$,

we obtain the steady-state solution x_{ss} (labelled by subindex ss).

In Subsection S1.3, we show that the correlations $\langle \hat{b}_v^\dagger \hat{b}_{v'} \rangle$ ($v \neq v'$) between the three main Raman-active vibrational modes considered in the main text are much smaller than their populations $\langle \hat{b}_v^\dagger \hat{b}_v \rangle$ because these vibrational modes are strongly detuned with respect to each other. In such a case, we can ignore the correlations in eqn (S29) and the equations for the population $\langle \hat{b}_v^\dagger \hat{b}_v \rangle$ become independent for each vibrational mode. The resulting equations correspond to eqn (1) in the main text.

S1.2 Expressions to Obtain the SERS Spectrum

In this subsection, we derive the expressions for the differential scattered SERS power $dP(\omega)/d\Omega$. In the classical electromagnetic theory of SERS⁸, $dP(\omega)/d\Omega$ is evaluated as $dP(\omega)/d\Omega = S(\omega)r^2$, where $S(\omega) = \frac{1}{2} \epsilon_0 c_0 \mathbf{E}^*(\mathbf{r}_d, \omega) \cdot \mathbf{E}(\mathbf{r}_d, \omega)$ is the time-averaged Poynting vector at the detector position \mathbf{r}_d (with $\frac{1}{2} (\mathbf{E}(\mathbf{r}_d, \omega) e^{-i\omega t} + \mathbf{E}^*(\mathbf{r}_d, \omega) e^{i\omega t})$ the total scattered field at the detector). Here r is the distance between the detector and the molecule. The result of $dP(\omega)/d\Omega$ for a detector at infinity does not depend on r because the scattered field decays as $1/r$. The differential Raman cross-section can be directly computed as $d\sigma/d\Omega = [dP/d\Omega]/I_{las}$, with $I_{las} = \frac{1}{2} \epsilon_0 c_0 E_0^2$ the laser intensity.

On the other hand, in the quantum description the differential scattered power in the stationary regime can be expressed as:

$$\frac{dP}{d\Omega} = 2\epsilon_0 c_0 r^2 \frac{1}{\pi} \text{Re} \int_0^\infty d\tau \langle \hat{\mathbf{E}}^\dagger(\mathbf{r}_d, \tau) \cdot \hat{\mathbf{E}}(\mathbf{r}_d, 0) \rangle e^{-i\omega\tau}, \quad (S33)$$

with $\hat{\mathbf{E}}(\mathbf{r}_d, \tau) + \hat{\mathbf{E}}^\dagger(\mathbf{r}_d, \tau)$ the electric field operator at the detector at time τ (note that, in contrast with the definition of the classical electric field, there is no $1/2$ prefactor in the definition of the electric field operator). Equation (S33) can be obtained by following Ref. 9 (eqn. (5.256)) and Ref. 10 (Appendix 10.D).

To evaluate eqn (S33), we derive the Heisenberg equation for the operator $\hat{\mathbf{E}}(\mathbf{r}_d, \tau)$ with the linearized optomechanical interaction Hamiltonian given in eqn (S4). Applying the Born-Markov approximation and using eqns (S14) to (S16), we can relate $\hat{\mathbf{E}}(\mathbf{r}_d, \tau)$ with the creation and annihilation operators of the molecular vibrations: $\hat{\mathbf{E}}(\mathbf{r}_d, \tau) \approx \frac{1}{2\epsilon_0} \sum_v \frac{\omega^2}{c_0^2} \overleftrightarrow{\mathbf{G}}(\mathbf{r}_d, \mathbf{r}_m; \omega) \cdot \mathbf{p}_v e^{-i\omega\tau} (\hat{b}_v(\tau) + \hat{b}_v^\dagger(\tau))$. Note that within these approximations, this operator explicitly includes the frequency ω . Inserting the expression of $\hat{\mathbf{E}}(\mathbf{r}_d, \tau)$ and its conjugate $\hat{\mathbf{E}}^\dagger(\mathbf{r}_d, \tau)$ into eqn (S33), we obtain the following expression for the differential scattered power¹:

$$\begin{aligned} \frac{dP}{d\Omega} &= \text{Re} \left\{ \sum_{v,v'} K_{vv'}(\omega) \left[S_{vv'}^{res,st}(\omega - \omega_l) + S_{vv'}^{res,as}(\omega - \omega_l) \right. \right. \\ &\quad \left. \left. + S_{vv'}^{off,st}(\omega - \omega_l) + S_{vv'}^{off,as}(\omega - \omega_l) \right] \right\}. \end{aligned} \quad (S34)$$

In this expression, the propagation factor is defined as

$$K_{vv'}(\omega) = \frac{c_0 r^2}{2\pi \epsilon_0} \mathbf{p}_v^* \cdot \left[\frac{\omega^2}{c_0^2} \overleftrightarrow{\mathbf{G}}^*(\mathbf{r}_d, \mathbf{r}_m; \omega) \right] \cdot \left[\frac{\omega^2}{c_0^2} \overleftrightarrow{\mathbf{G}}(\mathbf{r}_d, \mathbf{r}_m; \omega) \right] \cdot \mathbf{p}_{v'}, \quad (S35)$$

and the frequency-dependent spectral densities are given by

$$S_{\nu\nu'}^{res,st}(\omega) = \int_{-\infty}^{\infty} d\tau e^{-i\omega\tau} \theta(\tau) \langle \hat{b}_\nu(\tau) \hat{b}_{\nu'}^\dagger(0) \rangle, \quad (S36)$$

$$S_{\nu\nu'}^{res,as}(\omega) = \int_{-\infty}^{\infty} d\tau e^{-i\omega\tau} \theta(\tau) \langle \hat{b}_\nu^\dagger(\tau) \hat{b}_{\nu'}(0) \rangle, \quad (S37)$$

$$S_{\nu\nu'}^{off,st}(\omega) = \int_{-\infty}^{\infty} d\tau e^{-i\omega\tau} \theta(\tau) \langle \hat{b}_\nu(\tau) \hat{b}_{\nu'}(0) \rangle, \quad (S38)$$

$$S_{\nu\nu'}^{off,as}(\omega) = \int_{-\infty}^{\infty} d\tau e^{-i\omega\tau} \theta(\tau) \langle \hat{b}_\nu^\dagger(\tau) \hat{b}_{\nu'}^\dagger(0) \rangle. \quad (S39)$$

Equations (S36-S37) are the resonant contributions to the Stokes $S_{\nu\nu'}^{res,st}$ and anti-Stokes $S_{\nu\nu'}^{res,as}$ scattering, while eqns (S38-S39) are off-resonant contributions. Equations (S36-S39) correspond to the Fourier transform of the two-time correlations, $\langle \hat{b}_\nu(\tau) \hat{b}_{\nu'}^\dagger(0) \rangle$, $\langle \hat{b}_\nu^\dagger(\tau) \hat{b}_{\nu'}(0) \rangle$, $\langle \hat{b}_\nu(\tau) \hat{b}_{\nu'}(0) \rangle$, $\langle \hat{b}_\nu^\dagger(\tau) \hat{b}_{\nu'}^\dagger(0) \rangle$, respectively, where τ indicates the time difference from the steady state labeled by 0. $\theta(\tau)$ is the step function and ensures causality.

In the next step, we apply the quantum regression theorem¹¹. According to this theorem, the differential equations for $\langle \hat{b}_\nu \rangle$ are the same as for the two-time correlations $\langle \hat{b}_\nu(\tau) \hat{b}_{\nu'}^\dagger(0) \rangle$ and $\langle \hat{b}_\nu(\tau) \hat{b}_{\nu'}(0) \rangle$, and those for $\langle \hat{b}_\nu^\dagger \rangle$ are the same as those for the correlations $\langle \hat{b}_\nu^\dagger(\tau) \hat{b}_{\nu'}(0) \rangle$ and $\langle \hat{b}_\nu^\dagger(\tau) \hat{b}_{\nu'}^\dagger(0) \rangle$. The initial values of the two-time correlations are given by the steady-state values (again indicated by subindex *ss*) as $\langle \hat{b}_\nu(0) \hat{b}_{\nu'}^\dagger(0) \rangle = \langle \hat{b}_\nu \hat{b}_{\nu'}^\dagger \rangle_{ss} = \delta_{\nu\nu'} + \langle \hat{b}_\nu^\dagger \hat{b}_\nu \rangle_{ss}$, $\langle \hat{b}_\nu(0) \hat{b}_{\nu'}(0) \rangle = \langle \hat{b}_\nu \hat{b}_{\nu'} \rangle_{ss}$, and $\langle \hat{b}_\nu^\dagger(0) \hat{b}_{\nu'}(0) \rangle = \langle \hat{b}_\nu^\dagger \hat{b}_{\nu'} \rangle_{ss}$, $\langle \hat{b}_\nu^\dagger(0) \hat{b}_{\nu'}^\dagger(0) \rangle = \langle \hat{b}_\nu^\dagger \hat{b}_{\nu'}^\dagger \rangle_{ss}$.

In our system the off-resonant terms $\langle \hat{b}_\nu \hat{b}_{\nu'} \rangle_{ss}$, $\langle \hat{b}_\nu^\dagger \hat{b}_{\nu'}^\dagger \rangle_{ss}$ are orders of magnitude smaller than the resonant-terms $\langle \hat{b}_\nu^\dagger \hat{b}_{\nu'} \rangle_{ss}$ both for $\nu = \nu'$ and for $\nu \neq \nu'$, as confirmed by our calculations (not shown). Therefore the contributions $S_{\nu\nu'}^{off,st}(\omega)$ and $S_{\nu\nu'}^{off,as}(\omega)$ to the SERS spectrum can be ignored, which is analogue to the application of the rotating wave approximation. We can thus simplify the notation in the following by denoting $S_{\nu\nu'}^{res,k=st,as}(\omega)$ as $S_{\nu\nu'}^{k=st,as}(\omega)$, i.e., dropping the superscript "res". Using eqns (S31), (S32) and eqns (S36), (S37), we obtain

$$\sum_{\nu''} \left(\delta_{\nu\nu''} i(\omega + \tilde{\omega}_\nu) - i\nu_{\nu''\nu}^{(1)} \right) S_{\nu''\nu'}^{st}(\omega) = \delta_{\nu\nu'} + \langle \hat{b}_\nu^\dagger \hat{b}_{\nu'} \rangle_{ss}, \quad (S40)$$

$$\sum_{\nu''} \left(\delta_{\nu\nu''} i(\omega - \tilde{\omega}_\nu^*) + i\nu_{\nu''\nu}^{(2)} \right) S_{\nu''\nu'}^{as}(\omega) = \langle \hat{b}_\nu^\dagger \hat{b}_{\nu'} \rangle_{ss}, \quad (S41)$$

or, in matrix form, $M^{k=st,as} x^{k,\nu'} = \lambda^{k,\nu'}$, for efficient calculation. The elements of the vectors $x^{st,\nu'}$, $x^{as,\nu'}$, $\lambda^{st,\nu'}$, $\lambda^{as,\nu'}$ and of the matrices M^{st} , M^{as} are $x_\nu^{st,\nu'} = S_{\nu\nu'}^{st}(\omega)$, $x_\nu^{as,\nu'} = S_{\nu\nu'}^{as}(\omega)$, $\lambda_\nu^{st,\nu'} = \delta_{\nu\nu'} + \langle \hat{b}_\nu^\dagger \hat{b}_\nu \rangle_{ss}$, $\lambda_\nu^{as,\nu'} = \langle \hat{b}_\nu^\dagger \hat{b}_\nu \rangle_{ss}$, $M_{\nu\nu''}^{st} = \delta_{\nu\nu''} i(\omega + \tilde{\omega}_\nu) - i\nu_{\nu''\nu}^{(1)}$, and $M_{\nu\nu''}^{as} = \delta_{\nu\nu''} i(\omega - \tilde{\omega}_\nu^*) + i\nu_{\nu''\nu}^{(2)}$. The solutions are $x^{k,\nu'} = [M^k]^{-1} \lambda^{k,\nu'}$.

Last, taking into account that the off-diagonal elements $S_{\nu\nu'}^{k=st,as}(\omega)$ are negligible, we can simplify eqn (S34) as:

$$\frac{dP}{d\Omega} = \sum_{\nu} [K_{\nu\nu}^+ \text{Re}\{S_{\nu\nu}^{st}(\omega - \omega_\nu)\} + K_{\nu\nu}^- \text{Re}\{S_{\nu\nu}^{as}(\omega - \omega_\nu)\}], \quad (S42)$$

and eqns (S40) and (S41) as:

$$i(\omega + \tilde{\omega}_\nu - \nu_{\nu\nu}^{(1)}) S_{\nu\nu}^{st}(\omega) = 1 + \langle \hat{b}_\nu^\dagger \hat{b}_\nu \rangle_{ss}, \quad (S43)$$

$$i(\omega - \tilde{\omega}_\nu^* + \nu_{\nu\nu}^{(2)}) S_{\nu\nu}^{as}(\omega) = \langle \hat{b}_\nu^\dagger \hat{b}_\nu \rangle_{ss}, \quad (S44)$$

which can be solved to obtain

$$S_{\nu\nu}^{st}(\omega) = \left(1 + \langle \hat{b}_\nu^\dagger \hat{b}_\nu \rangle_{ss}\right) / \left[i(\omega + \tilde{\omega}_\nu - \nu_{\nu\nu}^{(1)})\right], \quad (S45)$$

$$S_{\nu\nu}^{as}(\omega) = \langle \hat{b}_\nu^\dagger \hat{b}_\nu \rangle_{ss} / \left[i(\omega - \tilde{\omega}_\nu^* + \nu_{\nu\nu}^{(2)})\right]. \quad (S46)$$

In the derivation of eqn (S42), we have replaced $K_{\nu\nu}(\omega)$ in eqn (S34) by

$$K_{\nu\nu}^\pm = K_{\nu\nu}(\omega_l \mp \omega_\nu) = \frac{c_0 r^2}{2\pi\epsilon_0} \left| \frac{(\omega_l \mp \omega_\nu)^2}{c_0^2} \overleftrightarrow{G}(\mathbf{r}_d, \mathbf{r}_m; \omega_l \mp \omega_\nu) \mathbf{p}_\nu \right|^2, \quad (S47)$$

since the Raman lines are typically much sharper than $K_{\nu\nu}(\omega)$, which depends on the comparatively broad plasmonic response.

By inserting eqn (S45) and (S46) into eqn (S42), we obtain the differential radiative power for the Stokes and anti-Stokes scattering:

$$\frac{dP^{st}}{d\Omega} = \sum_{\nu} \frac{K_{\nu\nu}^+ \gamma_\nu^+ / 2}{(\omega - \omega_\nu^+)^2 + (\gamma_\nu^+ / 2)^2} \left(1 + \langle \hat{b}_\nu^\dagger \hat{b}_\nu \rangle_{ss}\right), \quad (S48)$$

$$\frac{dP^{as}}{d\Omega} = \sum_{\nu} \frac{K_{\nu\nu}^- \gamma_\nu^- / 2}{(\omega - \omega_\nu^-)^2 + (\gamma_\nu^- / 2)^2} \langle \hat{b}_\nu^\dagger \hat{b}_\nu \rangle_{ss}. \quad (S49)$$

Here, we have used the expression of $\nu_{\nu\nu}^{(1)}$, $\nu_{\nu\nu}^{(2)}$ (found below eqn (S29)) and defined the frequencies of the Stokes $\omega_\nu^+ = \omega_l - \omega_\nu + \frac{1}{2}(\Omega_{\nu\nu}^+ + \Omega_{\nu\nu}^-)$ and anti-Stokes lines $\omega_\nu^- = \omega_l + \omega_\nu - \frac{1}{2}(\Omega_{\nu\nu}^- + \Omega_{\nu\nu}^+)$, as well as their line-widths $\gamma_\nu^+ = \gamma_\nu^- = \gamma_\nu + \Gamma_{\nu\nu}^{opt}$. We thus find that, when the correlations are negligible, it is possible to treat molecular vibrations as independent from each other in the calculation of the vibrational populations and the Raman spectrum. Equations (S48) and (S49) are the same as eqn (7) and (8) in the main text.

S1.3 Negligible Correlation of Vibrational Modes

The expressions developed in Section S1.1 and S1.2 suggest that quantum correlations $\langle \hat{b}_\nu^\dagger \hat{b}_{\nu'} \rangle_{ss}$ could be established between different vibrational modes ($\nu \neq \nu'$) and that these correlations could contribute to the SERS spectrum. However, according to eqn (S29), the steady-state correlations $\langle \hat{b}_\nu^\dagger \hat{b}_{\nu'} \rangle_{ss}$ are inversely proportional to $\kappa_{\nu\nu'} = i(\omega_\nu - \omega_{\nu'}) + (\gamma_\nu + \gamma_{\nu'})/2$, while the steady-state vibrational population $\langle \hat{b}_\nu^\dagger \hat{b}_\nu \rangle_{ss}$ is inversely proportional to $\kappa_{\nu\nu} = \gamma_\nu$. Since the three Raman-active vibrational modes of the BPT molecule considered here are far away from each other in frequency, i.e. $\omega_\nu - \omega_{\nu'} \gg (\gamma_\nu + \gamma_{\nu'})/2$, we expect that $|\kappa_{\nu\nu'}| \gg \kappa_{\nu\nu}$ (for $\nu \neq \nu'$) and then the correlations should be much smaller than the vibrational population. To verify this, we show in Fig. S1 the evolution of the vibrational population of the three vibrational modes, namely 1066 cm⁻¹ (blue solid lines), 1269 cm⁻¹ (red dashed lines), and 1586 cm⁻¹ (green dotted lines), as well as the imaginary part of the correlations between them (black solid,

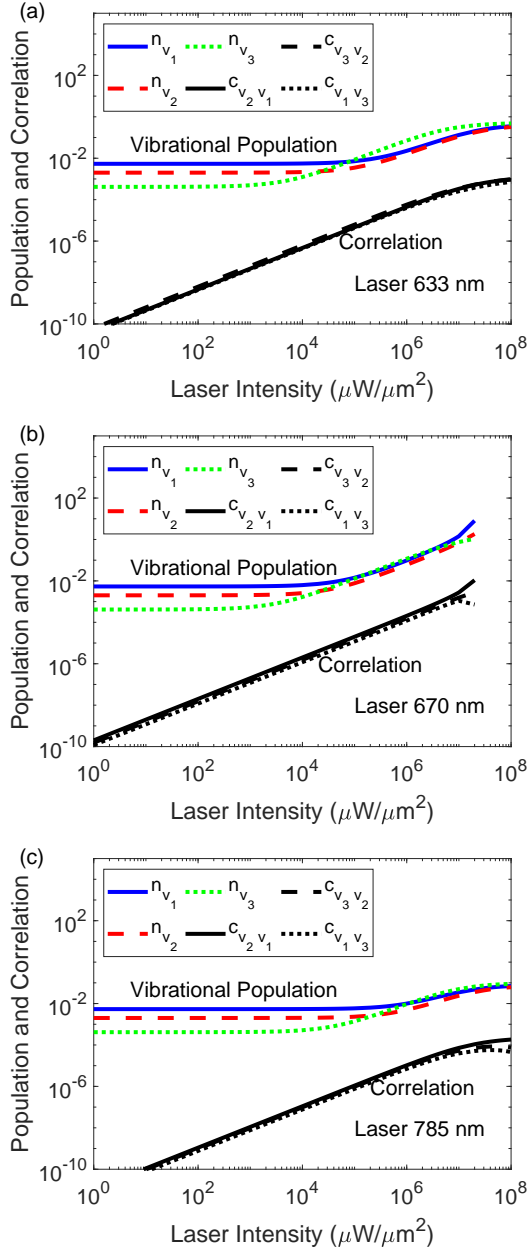


Fig. S1 Evolution of the vibrational population $n_v = \langle \hat{b}_v^\dagger \hat{b}_v \rangle$ of vibrational mode v , and imaginary part of the correlations $c_{v,v'} = \text{Im}[\langle \hat{b}_v^\dagger \hat{b}_{v'} \rangle]$ between vibrational modes v and v' , as a function of laser intensity I_{las} . The results are plotted for a laser wavelength of (a) 633 nm, (b) 670 nm and (c) 785 nm, considering the population of the three main vibrational modes of the BPT molecule with frequencies (blue solid lines) $\omega_{v_1} = 1066 \text{ cm}^{-1}$, (red dashed lines) $\omega_{v_2} = 1269 \text{ cm}^{-1}$ and (green dotted lines) $\omega_{v_3} = 1586 \text{ cm}^{-1}$. The black solid, dashed and dotted lines are the correlations $c_{v_2v_1}$, $c_{v_3v_2}$, $c_{v_1v_3}$ between pairs of these vibrational modes. The temperature is 293 K (room temperature) and other parameters are the same as those used in the main text.

dashed and dotted lines), as a function of laser intensity, and for laser wavelength 633 nm (a), 670 nm (b) and 785 nm (c). We focus on the imaginary part of the correlations because the real part cancels out in eqn (S29) for the vibrational populations. As expected, in all the cases considered, the correlations are orders of magnitude smaller than the vibrational population. We find

a similar result for the real part of the correlations (not shown). This result justifies ignoring the correlations when determining the vibrational population and the SERS spectrum, and thus allows us to consider vibrational modes independently, giving rise to the simplified expressions derived in the end of Section S1.1 and S1.2, and presented in the main text.

S2 Identification of the Dipolar Contribution in the Plasmonic Response

In this section we discuss in more detail the procedure to extract the contribution of the Bonding Dipolar Plasmon (BDP) mode to the plasmonic response, which was used in the main text to compare the single-mode and continuum-field results, and emphasize how the use of the former is often inaccurate. In the following, we first indicate the expressions of the local electric field and the dyadic Green's functions associated with the BDP mode. Then, we show that for the specific situation where the BDP mode dominates the response, these expressions result in formally identical expressions to those of the vibrational populations and the Raman scattering as in previous works which considered a single discrete plasmonic mode^{5,12,13}. Finally, we provide the technical details of the fitting in Section S2.1 and use the fitted values to extract important properties of the plasmonic resonance.

For the single BDP mode, the local field induced by the laser excitation at the position of the molecule \mathbf{r}_m can be expressed as $\frac{1}{2}[\mathbf{E}^s(\mathbf{r}_m, \omega) e^{-i\omega t} + \mathbf{E}^{s,*}(\mathbf{r}_m, \omega) e^{i\omega t}]$, where $\mathbf{E}^s(\mathbf{r}_m, \omega)$ adopts the following form:

$$\mathbf{E}^s(\mathbf{r}_m, \omega) = -\frac{\mathbf{E}^s(\mathbf{r}_m, \omega_c) i \kappa_c / 2}{\omega_c - \omega - i \kappa_c / 2}, \quad (\text{S50})$$

with ω_c and κ_c the frequency and the damping rate of the mode. We use the super-script 's' through this section to emphasize that we are dealing with the single-mode contribution. We can also write this equation as a function of the field enhancement K at resonance and laser amplitude $E_0 = |\mathbf{E}_0|$ as:

$$\mathbf{E}^s(\mathbf{r}_m, \omega) = -\frac{\mathbf{u}(\mathbf{r}_m) K E_0 i \kappa_c / 2}{\omega_c - \omega - i \kappa_c / 2}. \quad (\text{S51})$$

Here, the mode function $\mathbf{u}(\mathbf{r})$ is defined as the ratio of the electric fields at position \mathbf{r} to the maximum module of the electric fields in the gap. This function thus contains the information about the spatial field distribution and field polarization.

The near-field and far-field dyadic Green functions follow

$$\frac{\omega^2}{c_0^2} \overleftrightarrow{G}^s(\mathbf{r}_m, \mathbf{r}_m, \omega) \approx B \frac{\omega_c}{2} \frac{\mathbf{u}(\mathbf{r}_m) \otimes \mathbf{u}^*(\mathbf{r}_m)}{\omega_c - \omega - i \kappa_c / 2} \quad (\text{S52})$$

and

$$\frac{\omega^2}{c_0^2} \overleftrightarrow{G}^s(\mathbf{r}_d, \mathbf{r}_m, \omega) \approx C' \frac{\omega^2}{\omega_c^2} \frac{\mathbf{u}(\mathbf{r}_d) \otimes \mathbf{u}^*(\mathbf{r}_m)}{\omega_c - \omega - i \kappa_c / 2}, \quad (\text{S53})$$

respectively. For the comparison with previous work (see below), we can relate the proportionality factors B and C' with the properties of the cavity according to $B = \frac{1}{\epsilon_{gap} V_{eff}}$ and $C' \propto \frac{\omega_c^2}{r} \sqrt{\frac{\omega_c \kappa_c}{4 \hbar c_0 \epsilon_{gap} V_{eff}}}$. Here, the effective mode volume V_{eff} can be calculated as the total integrated electromagnetic energy of the mode normalized by twice the maximum energy of the electric fields at the gap of per-

mitivity ε_{gap} (see eqn (3) in Ref. 14) and r is the distance to the detector.

Introducing eqns. (S51)-(S53) into the eqns. (S22), (S23), and (S47) in section S1, we obtain:

$$\Omega_{vv}^{s,\pm} = \frac{1}{2\hbar\varepsilon_0} Q_v^0 \overleftrightarrow{R}_v \mathbf{E}^s(\mathbf{r}_m, \omega_l) \cdot \frac{\omega_c}{2\varepsilon_{gap} V_{eff}} \frac{\mathbf{u}(\mathbf{r}_m) \otimes \mathbf{u}^*(\mathbf{r}_m) (\omega_c - \omega)}{(\omega_c - (\omega_l \mp \omega_v))^2 + (\kappa_c/2)^2} Q_v^0 \overleftrightarrow{R}_v \mathbf{E}^{s,*}(\mathbf{r}_m, \omega_l), \quad (\text{S54})$$

$$\Gamma_{vv}^{s,\pm} = \frac{1}{2\hbar\varepsilon_0} Q_v^0 \overleftrightarrow{R}_v \mathbf{E}^s(\mathbf{r}_m, \omega_l) \cdot \frac{\omega_c}{2\varepsilon_{gap} V_{eff}} \frac{\mathbf{u}(\mathbf{r}_m) \otimes \mathbf{u}^*(\mathbf{r}_m) \kappa_c/2}{(\omega_c - (\omega_l \mp \omega_v))^2 + (\kappa_c/2)^2} \cdot Q_v^0 \overleftrightarrow{R}_v \mathbf{E}^{s,*}(\mathbf{r}_m, \omega_l) \quad (\text{S55})$$

for the optomechanical parameters and

$$K_{vv}^{s,\pm} \approx |r \sqrt{\frac{c_0}{2\pi\varepsilon_0}} C' \frac{(\omega_l \mp \omega_v)^2}{\omega_c^2} \frac{\mathbf{u}(\mathbf{r}_d) \cdot \mathbf{u}(\mathbf{r}_d)}{\omega_c - (\omega_l \mp \omega_v) - i\kappa_c/2} \times \mathbf{u}^*(\mathbf{r}_m) \cdot Q_v^0 \overleftrightarrow{R}_v \mathbf{E}^s(\mathbf{r}_m, \omega_l)|^2 \quad (\text{S56})$$

for the propagation factor.

By careful comparison^{12,14,15}, it can be seen that eqns. (S54)-(S56) are fully consistent with those in previous literature^{5,12,13}, which treated the single mode as a discrete resonance. We note that for this comparison we have ignored the optomechanical coupling-induced plasmon frequency shift and the difference between the coherent and incoherent vibrational populations since they are typically negligible for molecular optomechanics¹⁵

S2.1 Calculation of the Fitting Parameters for the Local Electric Field and the Dyadic Green's Function within the Single-mode Model

In this sub-section we discuss the fitting of the local electric field and of the dyadic Green's function implemented to extract the single mode contribution from the full complex plasmonic response. Since in our system the local electric field is mainly polarized along the z direction, normal to the gold substrate, and the Raman tensor is dominated by the zz -component due to the vertical molecular orientation, we focus on the E_z , G_{zz} and G_{jz} components of the local field and of the near-field and far-field dyadic Green's function, respectively. For this particular case, we obtain the following expressions from eqns (S50), (S52), and (S53):

$$\left| \frac{E_z^s(\mathbf{r}_m)}{E_0} \right| = \left| A \frac{\kappa_c/2}{\omega_c - \omega - i\kappa_c/2} \right|, \quad (\text{S57})$$

$$\frac{\omega^2}{c_0^2} G_{zz}(\mathbf{r}_m, \mathbf{r}_m, \omega) = B \frac{\omega_c/2}{\omega_c - \omega - i\kappa_c/2}, \quad (\text{S58})$$

$$\frac{\omega^4}{c_0^4} \sum_j |G_{jz}^s(\mathbf{r}_d, \mathbf{r}_m, \omega)|^2 = C \frac{\omega^4}{\omega_c^4} \frac{(\omega_c/2)^2}{(\omega_c - \omega)^2 + (\kappa_c/2)^2}, \quad (\text{S59})$$

with $C = C'/(\omega_c/2)^2$ in the last equation.

We fit simultaneously the results in Fig. 3 in the main text with

the output from eqns. (S57)-(S59) (see solid lines). We fit only the results for wavelengths larger than 650 nm, because higher order plasmonic modes, that are not included in the single-mode model, strongly affect the response for smaller wavelengths. Similarly, we only fit the imaginary part of the near-field dyadic Green's function, as the real part is also strongly influenced by the plasmonic pseudo-mode (Section S3). Further, we choose to fit the module of $E_z^s(\mathbf{r}_m)$ and not the phase as the former is the magnitude present in eqns (S54) and (S55) for the simplified single-mode description considered here. The fitting results are shown as blue and red solid lines in Fig. 3 of the main text. They agree very satisfactorily with the exact results from the continuum-field model (blue and red dots) around the wavelength of the BDP mode at 720 nm.

From these fittings, we can extract the single-mode plasmon frequency $\hbar\omega_c = 1.726$ eV, plasmon damping rate $\hbar\kappa_c = 0.136$ eV, as well as the following proportionality parameters: $A = 391$, $B = 2.09 \times 10^{-3} \text{ nm}^{-3}$ and $C = 5.22 \times 10^{-14} \text{ nm}^{-6}$. Furthermore, by assuming for simplicity a uniform mode function inside the NPoM nanocavity, i.e. $u_z(\mathbf{r}_m) \approx 1$, we can calculate the single-mode maximal field enhancement $K = 391$ from A , and the mode volume $V_{eff} = 227.5 \text{ nm}^3$ from B , according to the expressions of these coefficients after Eq.(S53). Once these parameters of the single mode are set, we can further determine other key parameters, as for instance the plasmon-laser coupling ($\hbar\Omega_{exc} = 2$ meV for $I_{las} = 1 \mu\text{W}/\mu\text{m}^2$) and the optomechanical coupling ($\hbar g_v = 0.032$ meV, 0.027 meV and 0.052 meV for the 1066 cm^{-1} , 1269 cm^{-1} and 1586 cm^{-1} vibrational mode, respectively). The exact definition and expressions for these parameters can be found in Ref. 12 and Ref. 14.

S3 Dyadic Green's Function of a Metal-Insulator-Metal Structure

Many features in the optomechanical parameters are associated with the contribution of the plasmonic pseudo-mode to the near-field dyadic Green's function $\overleftrightarrow{G}(\mathbf{r}_m, \mathbf{r}_m; \omega)$ in the NPoM nanocavity. At the same time, we have also pointed out that it is possible to explain the effect of the pseudo-mode on $\overleftrightarrow{G}(\mathbf{r}_m, \mathbf{r}_m; \omega)$ in terms of the optical response of a flat Metal-Insulator-Metal (MIM) configuration, which is the basic structure building up the NPoM gap. To support this statement, we compare $\overleftrightarrow{G}^{NPoM}(\mathbf{r}_m, \mathbf{r}_m; \omega)$ (more precisely, the zz -component along the direction normal to the substrate) of the NPoM nano-cavity and $\overleftrightarrow{G}^{MIM}(\mathbf{r}_m, \mathbf{r}_m; \omega)$ of a MIM structure formed by a dielectric spacer of the same thickness (1.3 nm) and relative permittivity ($\varepsilon_{gap} = 2.1$), as the NPoM gap. Consistent with the NPoM calculations (Section 4 in the main text), we only consider here the scattering field or, equivalently, the reflected field contribution of the dyadic Green's function, i. e. we do not include the contribution from the homogeneous infinite medium of relative permittivity ε_{gap} . To compute the dyadic Green's function of the MIM structure, we follow the procedure in Ref 16 and obtain G_{zz}^{MIM} for the position \mathbf{r} in the middle of the insulator layer from

$$G_{zz}^{MIM}(\mathbf{r}, \mathbf{r}; \omega) = \frac{i}{4\pi} \int_0^\infty dk_\rho f_{zz}^p(k_\rho), \quad (\text{S60})$$

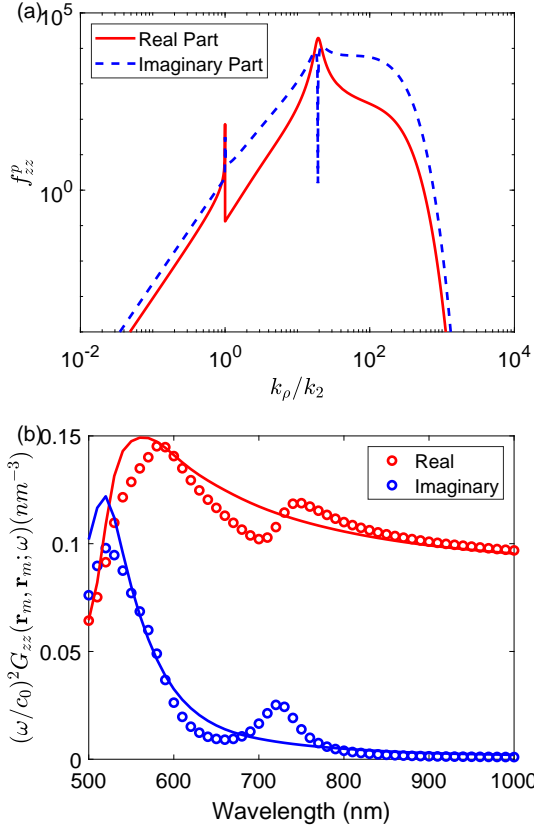


Fig. S2 Comparison of the dyadic Green's function of the NPoM and the MIM structure. (a) Dependence of the absolute value of the real part (red solid line) and imaginary part (blue dashed line) of $f_{zz}^p(k_\rho)$ for the Metal-Insulator-Metal (MIM) structure, as a function of the ratio of the radial wave number k_ρ to the wave-number in the middle layer k_2 for wavelength 633 nm. Here, we consider the absolute value of the real and imaginary parts in order to plot the results in logarithmic scale. The upper and lower layers of the MIM structure are infinitely-thick and made of gold and the middle insulator layer has a dielectric constant 2.1 and a height of $d = 1.3$ nm. (b) Comparison of the real (red) and imaginary (blue) part of the dyadic Green's function $G_{zz}(\mathbf{r}_m, \mathbf{r}_m; \omega)$ (multiplied by ω^2/c_0^2) for the molecule in the MIM structure (G_{zz}^{MIM} , solid lines) and the NPoM nano-cavity (G_{zz}^{NPoM} , circles) as a function of wavelength.

which is determined by the contribution of the p-polarized field:

$$f_{zz}^p(k_\rho) = \frac{k_\rho^3}{k_2^2 k_{2z}} \frac{2\mathcal{F}_p \exp(ik_2 d)}{1 - \mathcal{F}_p \exp(ik_2 d)}. \quad (\text{S61})$$

Here, $\mathcal{F}_p = \frac{\epsilon_1 k_{2z} - \epsilon_2 k_{1z}}{\epsilon_1 k_{2z} + \epsilon_2 k_{1z}}$ is the Fresnel reflection coefficient¹⁶, $k_l = \sqrt{\epsilon_l \omega/c_0}$ and $k_{lz} = \sqrt{k_l^2 - k_\rho^2}$ are the wavevector and its z component in the l -th layer of permittivity ϵ_l ($l = 1$ corresponding to any of the two metal layers and $l = 2$ to the dielectric layer), and k_ρ is the radial in-plane component of the wavevector (the same in all layers).

Figure S2 (a) shows the dependence of the real part (red solid line) and imaginary part (blue dashed line) of $f_{zz}^p(k_\rho)$ on the normalized radial wave-number k_ρ/k_2 , for wavelength $\lambda = 633$ nm. The very sharp singularity at $k_\rho = k_2$ appears because $k_{2z} = \sqrt{k_2^2 - k_\rho^2}$ in the denominator of eqn (S61) becomes zero. $k_\rho < k_2$ corresponds to propagating waves in the metal, and $k_\rho > k_2$ to

evanescent waves. Furthermore, there is also a maximum at much larger $k_\rho = k_{spp}$ because $1 - \mathcal{F}_p \exp(ik_2 d)$ (also in the denominator of eqn (S61)) becomes zero. Because $k_{spp} \gg k_2, k_1$, we have for this maximum $k_{2z} \approx k_{1z} \approx ik_\rho$, $|\mathcal{F}_p| \approx |\frac{\epsilon_1 - \epsilon_2}{\epsilon_1 + \epsilon_2}| \approx 1.4253$, and $k_{spp} \approx -\frac{1}{d} \ln |\mathcal{F}_p^{-1}| \approx 0.27 \text{ nm}^{-1}$. The field at $k_\rho \approx k_{spp}$ has an imaginary wave-number in the z-direction and can be identified as the surface plasmon mode. Last, there is an important contribution of the field due to the integration over large $k_\rho \gg k_{spp}$ components (i.e. $f_{zz}^p(k_\rho)$ remains large), which have been identified as localized surface wave modes¹⁷. For the MIM under consideration and a wavelength of $\lambda = 633$ nm in Fig. S2(a), the imaginary and real part of the dyadic Green's function are mostly determined by the surface plasmon mode and the surface wave modes¹⁷, respectively (note that the integral in eq. S60 is multiplied by i).

For the conditions of interest in this work, we can exploit the fact that the dyadic Green's function is mainly determined by the kernel $f_{zz}^p(k_\rho)$ at large k_ρ to obtain approximate solutions. We first obtain $f_{zz}^p \approx \frac{k_\rho^2}{ik_2^2} \frac{2\mathcal{F}_p \exp(-k_\rho d)}{1 - \mathcal{F}_p \exp(-k_\rho d)}$ by replacing $k_{2z} \approx k_{1z} \approx ik_\rho$, and then solve the integral in eqn (S60) to obtain the following analytical expression: $G_{zz}^{MIM}(\mathbf{r}, \mathbf{r}; \omega) \approx \text{Li}_3(\mathcal{F}_p) / (\pi d^3 k_2^2)$. Here, $\text{Li}_n(z) = \sum_{k=1}^{\infty} z^k / k^n$ is the polylogarithm function and the Fresnel reflection coefficient can be approximated as $\mathcal{F}_p \approx \frac{\epsilon_1 - \epsilon_2}{\epsilon_1 + \epsilon_2}$. We have verified that, for the results in this section, this analytical expression is a very good approximation to the numerical evaluation of the integral in eqn (S60). For the latter, we use Cauchy's integral theorem to transform the integral along the real radial wavenumber to an integral along the contour in the complex plane^{16,18}.

Figure S2 (b) compares the real part (red circles) and imaginary part (blue circles) of the dyadic Green's function (multiplied by ω^2/c_0^2) for the molecule in the NPoM nano-cavity with the corresponding results (red and blue lines) for the molecule in the MIM structure. The results of the NPoM show a relatively narrow feature near 720 nm due to the localized bonding dimer plasmon mode, which is thus not present for the MIM structure. Besides this difference, the results for the two structures under consideration agree well with each other. Notably, we observe that in both cases the imaginary part strongly increases for wavelengths ≤ 640 nm, and the real part presents a significant, approximately constant, contribution that extends over large wavelengths. These two features are key to understand many of the results in the main text which can be interpreted in terms of the coupling of the molecule with the MIM structure in the gap.

S4 Additional Numerical Results

In this section, we include and discuss additional numerical results which help to understand key aspects presented in the main text.

S4.1 Raman Tensor of Biphenyl-4-thiol Molecule

We have compared the Raman activity of the vibrational modes of an isolated biphenyl-4-thiol (BPT) molecule with the corresponding values of a BPT molecule bonded to a single gold atom (Fig. 2 in the main text). All the calculations of the Raman activity and Raman tensor components are performed within the Gaussian 16

Table S1 Raman tensor components of the three main Raman-active vibrational modes of a biphenyl-4-thiol molecule, in units of $\epsilon_0 \text{\AA}^2 \text{amu}^{-1/2}$.

$\omega_v (\text{cm}^{-1})$	R_{xx}	R_{xy}, R_{yx}	R_{xz}, R_{zx}	R_{yy}	R_{yz}, R_{zy}	R_{zz}
1066	-3.2	1.5	-7.4	-9.0	-0.2	-32.2
1269	4.1	0.6	15.5	7.4	-0.9	67.0
1586	-4.5	-1.5	-26.4	10.4	-1.2	113.0

Table S2 Atomic coordinates of the biphenyl-4-thiol molecule and the gold-bonded biphenyl-4-thiol molecule.

Biphenyl-4-thiol			Gold-bonded Biphenyl-4-thiol				
	x (Å)	y (Å)	z (Å)		x (Å)	y (Å)	z (Å)
C	1.66	-0.01	-0.02	C	-0.20	0.02	0.039
C	2.39	-1.13	0.43	C	0.53	-1.12	0.44
C	3.78	-1.11	0.48	C	1.92	-1.11	0.46
C	4.48	0.03	0.08	C	2.63	0.04	0.08
C	3.77	1.15	-0.37	C	1.91	1.18	-0.32
C	2.38	1.13	-0.42	C	0.52	1.16	-0.34
C	0.18	-0.04	-0.08	S	4.40	0.10	0.22
C	-0.58	1.10	0.24	C	-1.68	0.00	0.02
C	-1.98	1.08	0.19	C	-2.42	1.15	0.37
C	-2.66	-0.09	-0.19	C	-3.81	1.13	0.35
C	-1.91	-1.23	-0.51	C	-4.50	-0.02	-0.03
C	-0.52	-1.20	-0.45	C	-3.78	-1.17	-0.38
S	-4.43	-0.16	-0.27	C	-2.39	-1.15	-0.36
H	1.85	-2.02	0.76	H	0.00	-2.01	0.77
H	4.32	-1.98	0.84	H	2.47	-1.99	0.78
H	5.56	0.05	0.12	H	2.46	2.07	-0.63
H	4.31	2.04	-0.68	H	-0.01	2.04	-0.68
H	1.84	1.99	-0.80	Au	5.16	-0.67	-1.84
H	-0.08	2.00	0.56	H	-1.90	2.04	0.69
H	-2.53	1.98	0.45	H	-4.36	2.02	0.64
H	-2.42	-2.14	-0.81	H	-5.58	-0.03	-0.04
H	0.04	-2.09	-0.73	H	-4.30	-2.07	-0.69
H	-4.69	1.09	0.057	H	-1.84	-2.04	-0.67

package¹⁹. We observe an enhancement of the Raman activity due to the charge transfer between the BPT molecule and the single gold atom, i.e. a chemical enhancement^{20,21}. In Table 1 of the main text we provided the values of the components of the Raman tensor for the gold-bonded BPT molecule. To allow for a more direct estimation of the chemical enhancement, we provide here in Table S1 the components of the Raman tensor of the three Raman-active modes for the isolated BPT molecule. These Raman tensors are also used for the computation of the Raman scattering of the isolated BPT molecule in vacuum in Section 7.3 of the main text.

For the sake of completeness, in Table S2 we provide the atomic coordinates for the BPT molecule and the gold-bonded BPT molecule laying on the x-y plane, as used in our DFT calculations of the Raman tensor and the Raman activity. To obtain Table 1 in the main text and Table S1, we have rotated the molecules around the y-axis by the appropriate angles to ensure that they stand with an angle of 15 degree with respect to the z-axis, and that the side of the molecule with the sulfur atom is at the bottom.

S4.2 Identification of Plasmonic Modes based on the Near-field Maps

The scattering cross-section, the near-field enhancement and the far-field dyadic Green's function of the NPoM plasmonic nano-cavity (Fig. 3(a) and (c) in the main text), show peaks around 720 nm and 580 nm, which are identified in the main text as the Bonding Dipolar Plasmon (BDP) mode and the Bonding Quadruple Plasmon (BQP) mode, respectively. To confirm this assignment, we plot in Fig. S3 the near-field distribution corresponding to these modes in side-view (upper panels) and top-view (lower panels) cross-sections at the gap of the NPoM nano-cavity. In these plots, $x-z$ corresponds to the plane which contains the wavevector of incidence illumination, which is p-polarized with an angle of incidence of 55° with respect to the z -axis. The center of the gap is at $(x, y, z) = (0, 0, 0.65)$ nm. The size of the gap is 1.3 nm, and thus $z = 0$ and $z = 1.3$ nm define the points at the surface of the bottom metal and at the facet of the top metallic nanoparticle, respectively (see top panels of Fig. S3(a,b)).

The field induced in the gap is mostly polarized along the z -axis normal to the surface and its imaginary part is larger than its real part at the BDP and BQP resonances wavelength. We thus plot $\text{Im}\{E_z/E_0\}$, where we normalize the total local field by the amplitude E_0 of the incident field. Figure S3(a) shows that $\text{Im}\{E_z/E_0\}$ is almost constant inside the gap at the BDP wavelength (720 nm), but strongly decays outside. The induced surface charge density associated to this mode changes its sign between the nanoparticle surface and the substrate below, as schematically shown in the upper panel of Fig. S3(a) at a particular instant of time (positive charge at the bottom, and negative charge at the top). This field and charge distribution corresponds to the lowest-order capacitive polarization extended all over the gap, typical of the BDP

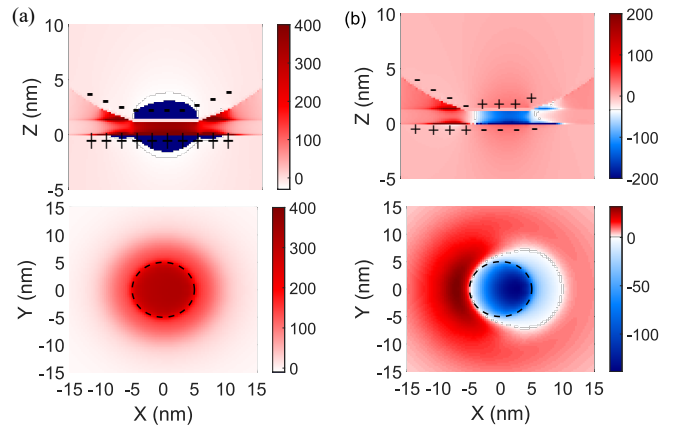


Fig. S3 Imaginary part of the enhancement of the z -component of the near-fields in a NPoM configuration induced by plane-wave laser illumination, $\text{Im}\{E_z/E_0\}$, relative to the incident amplitude E_0 . Upper panels show a side-view cross-section of the NPoM gap, and lower panels show its top-view cross-section. In (a) the bonding dipolar plasmon (BDP) mode is shown at a wavelength of 720 nm, and in (b) the bonding quadruple plasmon (BQP) mode at 580 nm. Both cross-sections contain the center of the gap. The plus and minus signs on the surfaces indicate the distribution of the positive and negative surface charge density associated with each mode. The incident angle of the plane-wave excitation relative to the normal of the substrate is 55° , as used in the main text.

mode. In contrast, the field enhancement $\text{Im}\{E_z/E_0\}$ for a wavelength of 580 nm shows two lobes of opposite sign in the gap (for negative and positive x coordinates) as expected for a BQP mode (the fields are not exactly anti-symmetric with respect to $x = 0$ because of retardation and the oblique illumination). The surface charge density distribution corresponding to this mode, shown in the upper panel of Fig. S3(b), indicates that the charges at the upper and lower metallic surfaces are of opposite sign, but this charge changes sign once along each surface, thus forming an overall quadrupole-like distribution. We last note that these fields and charge distributions are consistent with those found in similar configurations with a rigorous quasi-normal modes analysis in Ref. 22, in spite of the different criteria of modes classification.

S4.3 Optomechanical Parameters for the Intermediate-Frequency Vibrational Mode at 1269 cm^{-1}

In Fig. 4 of the main text, the dependence of the parameters Ω_{vv}^{\pm} and $\Gamma_{vv}^{\pm}, K_{vv}^{\pm}$ on the laser wavelength is shown for the low-frequency 1066 cm^{-1} and large-frequency 1586 cm^{-1} BPT vibrational modes. We plot in Fig. S4 the corresponding results for the intermediate-frequency 1269 cm^{-1} mode. The results in Fig. S4(a) and in Fig. 4(a) and (d) in the main text show that the dependence of Ω_{vv}^{\pm} on the laser wavelength is qualitatively similar for the three vibrational modes. This similarity occurs because the spectral dependence of Ω_{vv}^{\pm} is mostly due to (i) the local electric field at the illumination frequency, which is not affected by the change of the vibrational frequency, and (ii) the real part of the dyadic Green's function (affecting Ω_{vv}^{\pm}), which shows only a relatively weak dependence on the laser wavelength, as observed in Fig. 3(b) of the main text. Furthermore, also the propagators K_{vv}^+ and K_{vv}^- show a similar behavior for the 1269 cm^{-1} vibrational mode (Fig. S4(c)) when compared to the propagators of the other two vibrational modes (Fig. 4(c) and (f) in the main text). However, the exact position of the maxima (and shoulders) shift as the vibrational frequency ω_v changes. The moderate dependence of K_{vv}^+ and K_{vv}^- on the vibrational frequency ω_v can be explained by the small change produced in the evaluation frequency of the far-field dyadic Green's function $\overleftrightarrow{G}(\mathbf{r}_d, \mathbf{r}_m; \omega)$, at $\omega_l - \omega_v$ and $\omega_l + \omega_v$, respectively.

In contrast, when comparing Fig. S4 (b) with Fig. 4(b) and (e) in the main text, one finds that the relative strength of the vibrational pumping rate Γ_{vv}^+ with respect to the damping rate Γ_{vv}^- strongly depends on the vibrational frequency. Notably, the large dependence of Γ_{vv}^- on the vibrational frequency is mostly due to the proportionality of this parameter with the imaginary part of the near-field dyadic Green's function at the anti-Stokes frequency. The latter strongly increases for wavelengths smaller than $\approx 650 \text{ nm}$ due to the contribution of the plasmonic pseudo-mode. The actual frequency where the near field is evaluated directly depends on the frequency of the particular vibrational mode, thus the energy of the vibration strongly influences the value of Γ_{vv}^- . As a consequence, we find, for example, that the window range where the vibrational pumping rate Γ_{vv}^+ is larger than the damping rate Γ_{vv}^- , shrinks from $[654.7 \text{ nm}, 705.4 \text{ nm}]$ for the low-frequency 1066 cm^{-1} vibrational mode (Fig. 4(b) in the

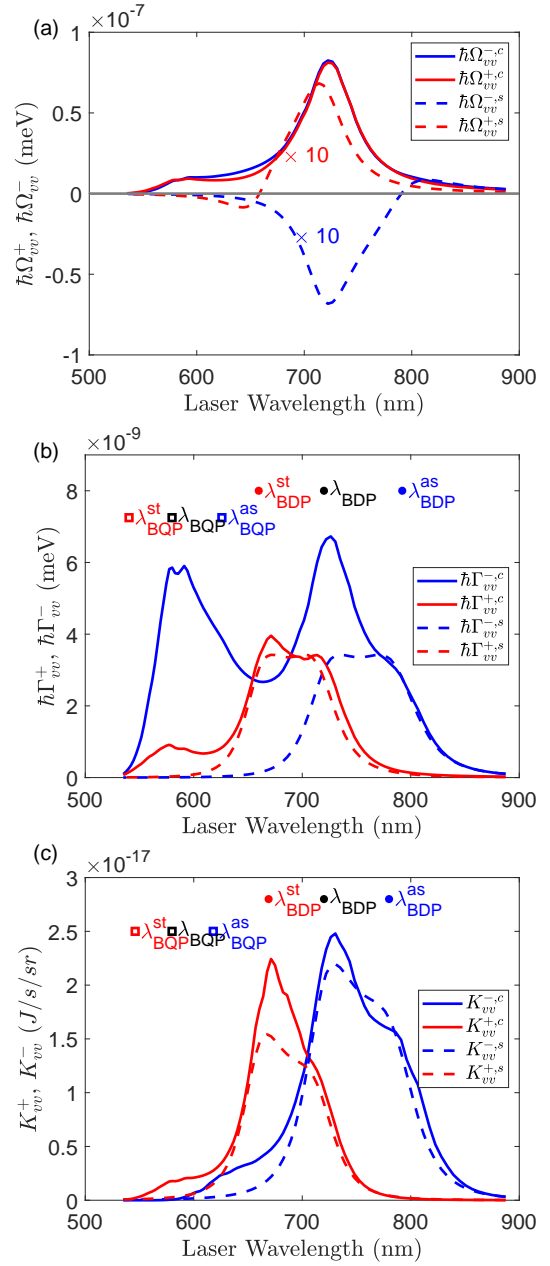


Fig. S4 Dependence of the optomechanical parameters (a) Ω_{vv}^{\pm} , (b) Γ_{vv}^{\pm} and (c) K_{vv}^{\pm} on the laser wavelength for the 1269 cm^{-1} vibrational mode of the BPT molecule. These calculations complete the results shown in Fig. 4 of the main text for the other two vibrational modes of this molecule. The blue lines correspond to Ω_{vv}^- , Γ_{vv}^- and K_{vv}^- (related to the anti-Stokes scattering) and the red lines to Ω_{vv}^+ , Γ_{vv}^+ and K_{vv}^+ (related to the Stokes scattering). The solid and dashed lines show results obtained within the continuum-field model and the single-mode model, respectively. The labels $\lambda_{\text{BDP},\text{BQP}}^{\text{st}}$, $\lambda_{\text{BDP},\text{BQP}}^{\text{as}}$ and $\lambda_{\text{BDP},\text{BQP}}^{\text{st}}$ are equivalent to the definition in Fig. 4 of the main text. In (a) the blue and red dashed lines are scaled by a factor of 10. Other parameters are the same as in Fig. 4 of the main text.

main text) to $[654.3 \text{ nm}, 689.7 \text{ nm}]$ for the intermediate-frequency 1269 cm^{-1} mode (Fig. S4 (b)), and that no such window exists for the large-frequency 1586 cm^{-1} mode (Fig. 4(e) in the main text), as the pseudomode affects more strongly the latter.

S4.4 Evolution of the Integrated Stokes Intensity for the Low-Frequency Vibrational Mode at 1066 cm^{-1}

Figure S5 compares the evolution of the integrated Stokes intensity S^{st} with increasing laser intensity I_{las} for the low-frequency vibrational mode at 1066 cm^{-1} , as obtained from the single-mode model (dashed lines) and from the continuum-field model (solid lines) at different incident laser wavelengths. This figure thus completes the results of the vibrational population and the integrated anti-Stokes intensity S^{as} shown in Fig. 6 (a) and (b) of the main text for the same vibrational mode.

The main difference between the evolution of S^{as} and S^{st} is that S^{as} is proportional to the vibrational population $\langle \hat{b}_v^\dagger \hat{b}_v \rangle$, i.e. $S^{as} = \pi K_{vv}^- \langle \hat{b}_v^\dagger \hat{b}_v \rangle$, while S^{st} depends on $1 + \langle \hat{b}_v^\dagger \hat{b}_v \rangle$, i.e. $S^{st} = \pi K_{vv}^+ (1 + \langle \hat{b}_v^\dagger \hat{b}_v \rangle)$. In the thermal regime, $\langle \hat{b}_v^\dagger \hat{b}_v \rangle$ is dominated by the thermal population n_v^{th} , which is typically much smaller than 1, making the Stokes signal much stronger than the anti-Stokes signal.

Furthermore, in the vibrational pumping regime, the vibrational population $\langle \hat{b}_v^\dagger \hat{b}_v \rangle \approx n_v^{th} + \Gamma_{vv}^+ / \gamma_v$ acquires an extra contribution Γ_{vv}^+ / γ_v that scales linearly with I_{las} (because the vibrational pumping rate Γ_{vv}^+ is proportional to I_{las}), and is added to the thermal vibrational population. Taking into account that $K_{vv}^\pm \propto I_{las}$, both S^{as} and S^{st} can thus potentially scale super-linearly or quadratically with I_{las} . This non-linear scaling can be observed for the anti-Stokes scattering when Γ_{vv}^+ / γ_v is comparable to the relatively small thermal vibrational population $n_v^{th} \approx 5.4 \times 10^{-3}$ (at room temperature), but to observe it in the Stokes scattering, Γ_{vv}^+ / γ_v needs to be similar to 1. Thus, the quadratic scaling can only be observed in the Stokes scattering for much larger laser in-

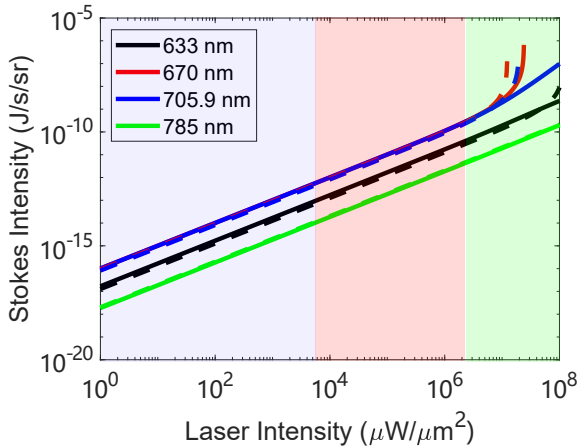


Fig. S5 Evolution of the integrated Stokes intensity for the 1066 cm^{-1} vibrational mode of the BPT molecule as a function of laser intensity I_{las} at incident laser wavelengths of 633 nm (black lines), 670 nm (red lines), 705.9 nm (blue lines) and 785 nm (green lines). The solid lines correspond to the results obtained with the continuum-field model and the dashed lines to those obtained with the single-mode model. The light blue, red and green background colors indicate the approximate laser intensity range for the thermal regime (weak I_{las}), the vibrational pumping regime (moderate I_{las}) and the regime of large laser intensity, respectively. Other parameters are the same as those in Fig. 6 of the main text.

tensity than in the anti-Stokes scattering. However, for such large I_{las} , the system enters into the regime of high intensity where other effects can strongly modify the results (e.g. the divergence of the SERS due to parametric instability, illustrated by the red solid line in Fig. S5). It is thus often challenging to distinguish the quadratic scaling of the Stokes scattering, for instance in the red solid line of Fig. S5, from other effects, except for specific laser wavelengths that lead to zero or very small effective optomechanical damping rate ($\Gamma_v^{opt} \approx 0$; blue solid line in Fig. S5). We notice that for 633 nm and 785 nm (black and green solid lines) the signal scales approximately linearly with laser intensity for all I_{las} considered because of the saturation of the vibrational population for very intense illumination.

Significantly, the Stokes and anti-Stokes emission show similar trends as I_{las} becomes very large. Thus, for the regime of large intensity where the main optomechanical effects of interest occur, the results and discussion about the anti-Stokes scattering addressed in the main text also apply to the Stokes scattering.

S4.5 Laser Threshold to Reach the Vibrational Pumping Regime

In Section 7 of the main text, we have discussed the laser threshold intensity $I_{thr,1}$ required to achieve the vibrational pumping regime. Note that $I_{thr,1}$ is defined as the laser intensity for which the vibrational population induced by the laser equals the thermal population. In Fig. S6, we investigate further the dependence of $I_{thr,1}$ on (a) the laser wavelength at room temperature $T = 293 \text{ K}$ and (b) the temperature for a given laser wavelength of 710 nm. We plot the results for the low-frequency vibrational mode at 1066 cm^{-1} (red lines) and for the large-frequency one at 1586 cm^{-1} (blue lines). We observe that $I_{thr,1}$ is smaller for a laser wavelength range of [650 nm, 710 nm] due to the relatively larger vibrational pumping rate (see Fig. 4(b) and (e) in the main text). Importantly, $I_{thr,1}$ is about ten times smaller for the 1586 cm^{-1} vibrational mode because this mode is characterized by a larger Raman tensor, and also by a smaller thermal vibrational population. The threshold values $I_{thr,1}$ obtained are challenging to reach with continuous-wave (CW) lasers but might be achievable with pulsed lasers.

Furthermore, Fig. S6 (b) shows that for both the vibrational modes at 1066 cm^{-1} (red lines) and at 1586 cm^{-1} (blue lines), the threshold intensity $I_{thr,1}$ can be dramatically decreased by reducing the temperature, in a way that $I_{thr,1}$ is at reach of CW lasers. This is the case not only for a relatively small vibrational decay rate $\hbar\gamma_v = 0.07 \text{ meV}$, as used through the paper (solid lines), but also for a much larger vibrational decay rate $\hbar\gamma_v = 2.5 \text{ meV}$ (dashed lines). In short, the conditions to experimentally demonstrate vibrational pumping²⁵ in molecular optomechanics are at reach by careful optimization of the incident laser conditions, temperature of operation, molecular Raman activity, and specifics of the plasmonic cavity.

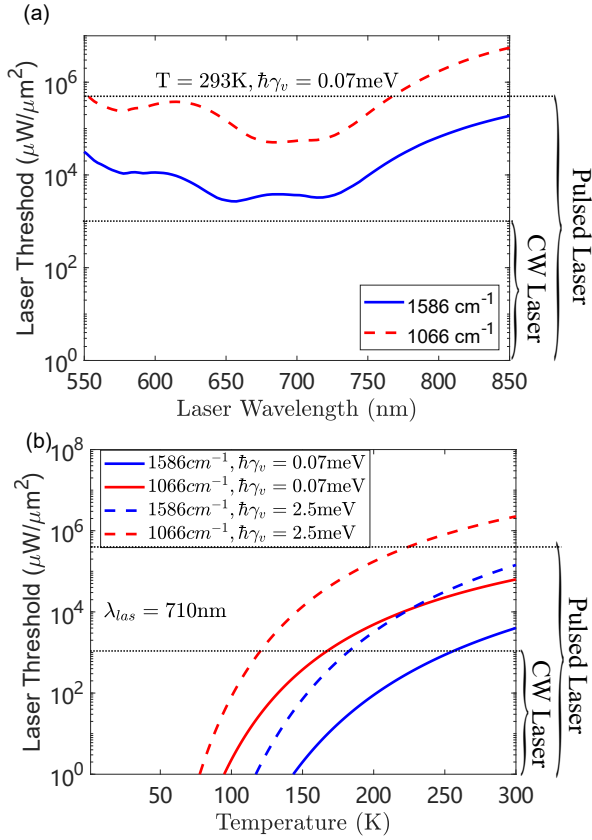


Fig. S6 Estimated laser threshold intensity $I_{thr,1}$ to achieve the vibrational pumping regime for the 1066 cm^{-1} (red line) and the 1586 cm^{-1} (blue line) vibrational modes. Panel (a) shows $I_{thr,1}$ as a function of laser wavelength at a temperature $T = 293\text{ K}$ (room temperature), with intrinsic vibrational decay rate $\hbar\gamma_v = 0.07\text{ meV}$. Panel (b) shows $I_{thr,1}$ as a function of temperature for laser wavelength 710 nm and two intrinsic vibrational decay rates, $\hbar\gamma_v = 0.07\text{ meV}$ and 2.5 meV . All the other parameters are the same as in Fig. 6 of the main text. We indicate the intensity values typically achievable in current experiments with continuous-wave (CW)^{23,24} and pulsed²⁴ laser illumination, as marked on the right-hand side of the panels.

S4.6 Laser Threshold to Reach the Parametric Instability and Saturation of the Vibrational Population

The saturation of the vibrational population and the parametric instability are achieved when the absolute value of the effective optomechanical damping rate becomes comparable to the intrinsic vibrational decay rate, i.e. $|\Gamma_v^{opt}| \approx \gamma_v$. This condition defines the laser threshold $I_{thr,2}$ to achieve these effects, as discussed in the main text. The dependence of $I_{thr,2}$ on laser wavelength within the continuum-field (solid lines) and single-mode (dashed lines) models is shown in Fig. S7 for (a) the 1066 cm^{-1} and (b) the 1586 cm^{-1} vibrational modes, where the blue-(red-)colored sections of each line indicate the illumination wavelengths that lead to parametric instability (saturation of the vibrational population).

Figure S7 (a) shows that, for the 1066 cm^{-1} vibrational mode, and according to the continuum-field model (solid lines), the parametric instability (blue-colored section of the solid line) can be achieved at a small range of laser wavelengths around 670 nm for the 1066 cm^{-1} vibrational mode, and the saturation of the vibrational population (red-colored sections) takes place outside

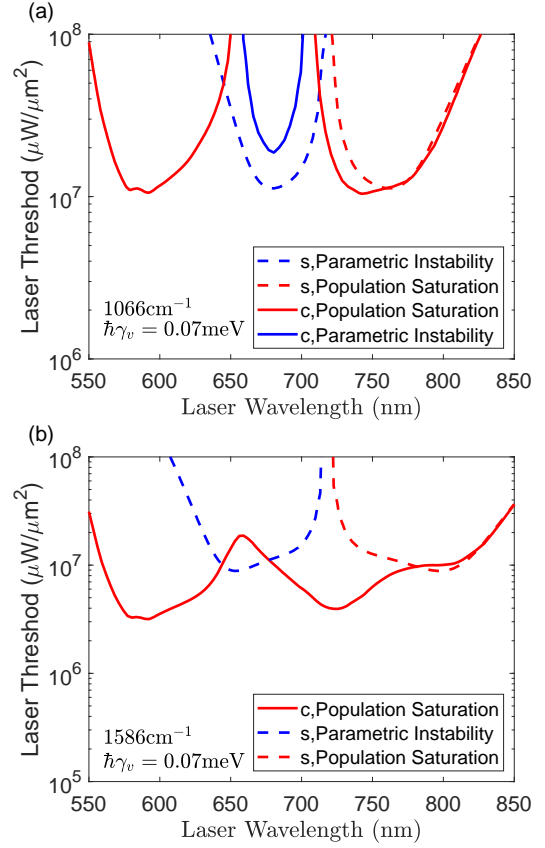


Fig. S7 Laser threshold intensity $I_{thr,2}$ to achieve parametric instability or saturation of the vibrational population for (a) the 1066 cm^{-1} and (b) the 1586 cm^{-1} vibrational modes, as predicted by the continuum-field model (solid lines, labeled "c") and by the single-mode model (dashed lines, labeled "s"). The color of the different section of the lines indicate the laser wavelengths at which the parametric instability (sections in blue) or the saturation of the vibrational population (sections in red) occur. The intrinsic vibrational decay rate is set to $\hbar\gamma_v = 0.07\text{ meV}$. All the other parameters are the same as in Fig. 6 of the main text.

this wavelength range. The minimum laser threshold for these two effects to occur is $1.87 \times 10^7 \mu W/\mu m^2$ for a laser wavelength of 680.6 nm , and $1.04 \times 10^7 \mu W/\mu m^2$ for 742.4 nm . On the other hand, the single-mode model (dashed lines) predicts the parametric instability and the saturation of the vibrational population for laser wavelengths smaller and larger than 720 nm , respectively. The more dramatic difference between the two models occurs for laser wavelengths smaller than 650 nm , where the continuum-field model predicts the saturation of the vibrational population for laser thresholds comparable to those found for other laser wavelengths, but the single-mode model suggests that the parametric instability is reached for an extremely large value of the laser threshold.

Figure S7 (b) shows that for the 1586 cm^{-1} vibrational mode, and within the continuum-field model (solid line), the saturation of the vibrational population is expected for all laser wavelengths considered (i.e. absence of parametric instability), and the minimum laser threshold is $3.17 \times 10^6 \mu W/\mu m^2$. This threshold is about 3 times smaller than that of the 1066 cm^{-1} vibrational mode because the Raman tensor is significantly larger for the former. In

contrast, within the single-mode model (dashed line), the trend remains similar as for the 1066 cm^{-1} vibrational mode: the parametric instability is obtained for laser wavelengths smaller than 720 nm, and the vibrational population saturation for larger ones.

S4.7 Comparison with the Classical SERS Theory

In Fig. 7 of the main text, we study the dependence of the SERS enhancement on the laser wavelength in different laser intensity regimes for the 1586 cm^{-1} vibrational mode. In Fig. S8, we compare the results for this mode in the thermal regime as obtained within the continuum-field model (blue and red solid lines) and as obtained according to classical electromagnetic theory of SERS (blue and red dashed lines)⁸.

In the classical theory of SERS, the enhancement factors EF_v^+ and EF_v^- of single-molecule Stokes and anti-Stokes scattering, respectively, for a given vibrational mode of frequency ω_v , are typically estimated following the well-known recipe of the fourth power of the local field enhancement⁸, (consistent with the reciprocity theorem) as:

$$EF_v^\pm = \frac{|\mathbf{E}_{loc}(\mathbf{r}_m, \omega_l \mp \omega_v) \cdot \overleftrightarrow{\mathbf{R}}_v^b \cdot \mathbf{E}_{loc}(\mathbf{r}_m, \omega_l)|^2}{|\mathbf{E}_{inc}(\mathbf{r}_m, \omega_l \mp \omega_v) \cdot \overleftrightarrow{\mathbf{R}}_v^i \cdot \mathbf{E}_{inc}(\mathbf{r}_m, \omega_l)|^2}, \quad (\text{S62})$$

where $\mathbf{E}_{loc}(\mathbf{r}_m, \omega_l)$ represents the local electric field induced by an incident laser of amplitude $|\mathbf{E}_{inc}(\mathbf{r}_m, \omega_l)|$. The enhancement $|\mathbf{E}_{loc}(\mathbf{r}_m, \omega_l)|/|\mathbf{E}_{inc}(\mathbf{r}_m, \omega_l)|$ approximately corresponds to the results in Fig. 3 (a) of the main text. $\overleftrightarrow{\mathbf{R}}_v^i$ and $\overleftrightarrow{\mathbf{R}}_v^b$ are the Raman tensor of the isolated molecule and that of the molecule bonded to a gold atom (to account for the chemical enhancement), respectively.

Figure S8 shows that the order of magnitude and the spectral dependence of the Stokes (red lines) and anti-Stokes (blue lines) SERS enhancement calculated from the continuum-field molecular optomechanics description (solid lines) agree very well

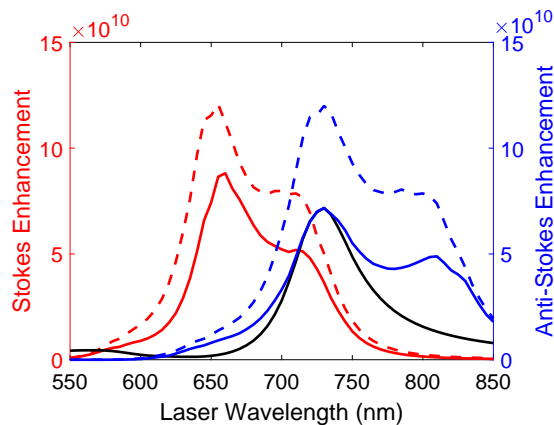


Fig. S8 Enhancement of the Stokes (red lines, left axis) and anti-Stokes scattering (blue lines, right axis) as a function of laser wavelength for the 1586 cm^{-1} vibrational mode, and weak laser intensity $I_{las} = 1 \mu\text{W}/\mu\text{m}^2$ (thermal regime). The solid and dashed lines are results based on the continuum-field model and on classical SERS theory, respectively, and the black solid line is the far-field scattering cross-section (scaled by a constant factor for easier comparison). Other parameters are the same as in Fig. 7 of the main text.

with the classical results obtained by applying eqn (S62) (dashed lines). The differences between both results can be associated to the fact that eqn (S62) is obtained from the application of the optical reciprocity theorem^{8,26}, which in our configuration is not exactly fulfilled, as the far field is evaluated at 1 μm from the NPoM structure.

For comparison, we also show in Fig. S8 the spectral shape of the far-field scattering cross-section (black solid line). We observe that this does not match the SERS enhancement but it shows a clear similarity, in particular when compared with the enhancement of the anti-Stokes scattering near 720 nm, the wavelength of the BDP mode. Thus, in the thermal regime, the scattering cross-section can serve as a useful guide to qualitatively predict the dependence of the SERS enhancement on the laser wavelength, as typically implemented in many experiments^{27,28}. Nevertheless, as shown in this work, care is needed when describing SERS enhancement in complex plasmonic systems^{29,30}.

S4.8 SERS Enhancement of the 1066 cm^{-1} Vibrational Mode

In Fig. 7 of the main text and in Fig. S8, we have studied the SERS enhancement of the 1586 cm^{-1} vibrational mode as a function of the wavelength of the excitation laser. In Fig. S9 we complete these results with those for the 1066 cm^{-1} vibrational mode, to illustrate the effects produced when considering a smaller vibrational frequency.

Figure S9 (a) shows that the Stokes (red lines) and anti-Stokes (blue lines) SERS enhancement for the 1066 cm^{-1} vibrational mode is dominated by a broad spectral maximum in the thermal regime (weak laser intensity, $I_{las} = 1 \mu\text{W}/\mu\text{m}^2$), similar to the 1586 cm^{-1} vibrational mode. The enhancement in this regime is mostly dominated by the propagation factors $K_{vv}^{+,-}$ (see Fig. 4(c) and (f) in the main text), which depend only moderately on the vibrational frequency. The main difference is that the Raman emission for the 1586 cm^{-1} vibrational mode shows two clear peaks, which gradually merge into one as the vibrational frequency becomes smaller.

In the vibrational pumping regime (moderate laser intensity, $I_{las} = 10^5 \mu\text{W}/\mu\text{m}^2$), the general trends are also independent of the vibrational frequency. The Stokes peak remains broad but the anti-Stokes enhancement is sharper, as shown in Fig. S9 (b) for the 1066 cm^{-1} vibrational mode, and in Fig. 7(b) of the main text for the 1586 cm^{-1} one. This behavior occurs because the anti-Stokes is proportional to the vibrational population, which in the regime considered here increases more dramatically for laser wavelengths around 720 nm.

The value of the vibrational frequency becomes very important in the regime of large laser intensity I_{las} . Figure S9 (c) shows that for $I_{las} = 1.5 \times 10^7 \mu\text{W}/\mu\text{m}^2$, the dependence of the SERS enhancement on the laser wavelength becomes sharper for the 1066 cm^{-1} vibrational mode, which differs from the spectrally-broad enhancement peak shown in Fig. 7(c) of the main text for the 1586 cm^{-1} vibrational mode. This difference is a direct consequence of the behavior of the effective optomechanical damping rate Γ_v^{opt} discussed in Section 6 of the main text. Γ_v^{opt} is positive at all laser wavelengths for the 1586 cm^{-1} vibrational mode,

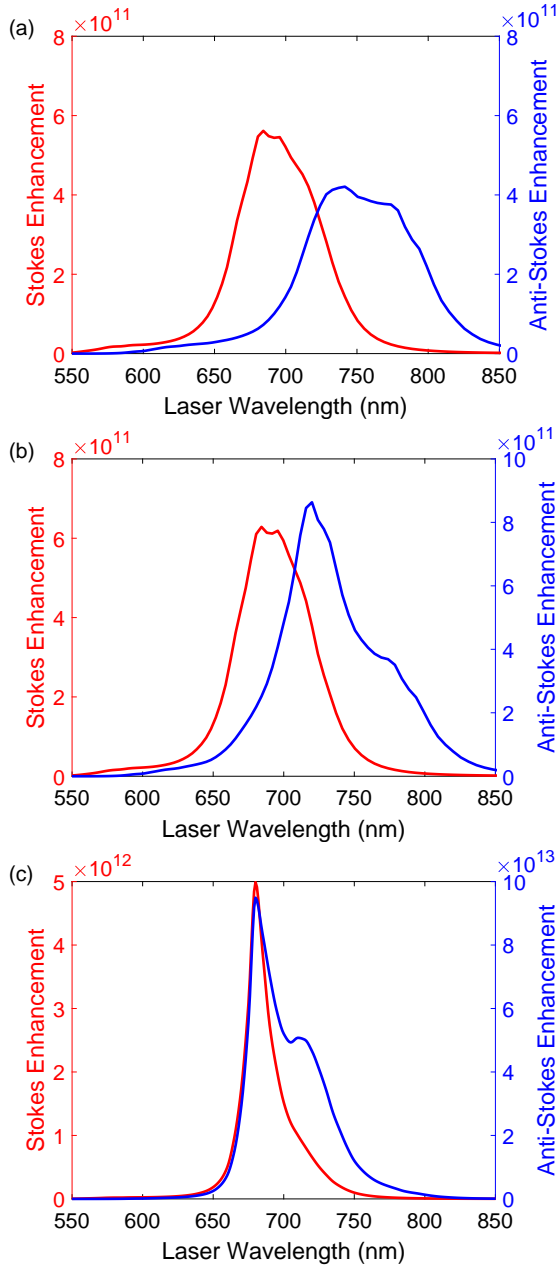


Fig. S9 Dependence of the Stokes (red lines, left axis) and anti-Stokes (blue lines, right axis) enhancement on the laser wavelength, for the 1066 cm^{-1} vibrational mode and a laser intensity (a) $I_{las} = 1 \mu\text{W}/\mu\text{m}^2$, (b) $I_{las} = 10^5 \mu\text{W}/\mu\text{m}^2$ and (c) $I_{las} = 1.5 \times 10^7 \mu\text{W}/\mu\text{m}^2$. These results are the counterpart of those in Fig. 7 of the main text for the 1586 cm^{-1} vibrational mode. Other parameters are the same as in Fig. 7 of the main text.

so that increasing the laser intensity always leads to the saturation of the vibrational population. However, for the 1066 cm^{-1} vibrational mode, a wavelength window exists where $\Gamma_v^{opt} < 0$. In this window the signal increases non-linearly for sufficiently large intensity until the response becomes divergent (parametric instability). A larger negative $\Gamma_v^{opt} < 0$ leads to a faster non-linear increase, which results in the spectral sharpening shown in Fig. S9 (c).

S4.9 Optomechanical Parameters of the Molecule in Vacuum

In Section 7.3 of the main text and Section S4.7 and S4.8, we have studied the enhancement of the Raman scattering, which requires the normalization of the Raman signal of the molecule in the NanoParticle-on-a-Mirror (NPoM) gap to the signal for a molecule in vacuum (or air). For this comparison, we need to obtain the optomechanical parameters of the molecule in vacuum. We show the dependence of the optomechanical parameters on the laser wavelength in Fig. S10 for the 1066 cm^{-1} vibrational mode with a laser intensity $I_{las} = 1 \mu\text{W}/\mu\text{m}^2$. For these calculations, we have used the values of the Raman tensor of the molecule in vacuum from Table S1. The actual frequencies of the vibrational modes of the molecule in vacuum are slightly shifted with respect to those of the molecule bonded to gold, however, the difference is so small that we neglect it in this normalization, and consider the original frequencies of the vibrations when bonded to gold. Figure S10 (a) shows that the vibrational damping rate Γ_{vv}^- (blue dashed line) is always larger than the vibrational pumping rate Γ_{vv}^+ (red solid line), and that both become smaller with increasing laser wavelength. The vibrational pumping and damping rates in

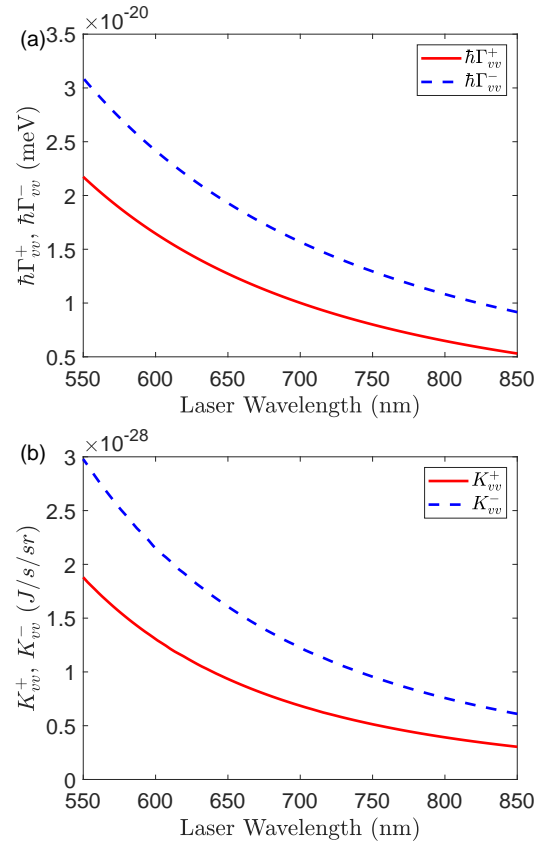


Fig. S10 Optomechanical parameters for an isolated BPT molecule in vacuum for the vibrational mode with wave-number 1066 cm^{-1} . (a) shows the vibrational pumping rate Γ_{vv}^+ (red solid line) and damping rate (blue dashed line) Γ_{vv}^- as a function of laser wavelength. (b) shows the propagation factors K_{vv}^+ (red solid line) and K_{vv}^- (blue dashed line) related to the Stokes and anti-Stokes scattering, respectively. The laser intensity is $I_{las} = 1 \mu\text{W}/\mu\text{m}^2$ and other parameters are the same as in Fig. 4 in the main text.

vacuum are related to the Stokes and anti-Stokes scattering in the vacuum field. In particular, we find that both optomechanical parameters are of the order of 10^{-20} meV in vacuum, which is about 11 to 12 orders of magnitude smaller than those when the NPoM is present (Fig. 4(b)).

On the other hand, Fig. S10 (b) shows the propagation factors $K_{\nu\nu}^+$ and $K_{\nu\nu}^-$ of the Stokes and anti-Stokes scattering, respectively, for the molecule in vacuum. $K_{\nu\nu}^\pm$ behaves similarly as $\Gamma_{\nu\nu}^\pm$ in this situation. $K_{\nu\nu}^-$ (blue dashed line) is larger than $K_{\nu\nu}^+$ (red solid line) and both get smaller as the laser wavelength increases. The values of $K_{\nu\nu}^\pm$ are of the order of 10^{-28} J/s/sr, and this is enhanced by 11 orders of magnitude in the presence of the NPoM, as observed by comparing Fig. S10 (b) with Fig. 4(c) in the main text. We do not study the vibrational frequency shifts $\Omega_{\nu\nu}^\pm$ because they are infinite, due to the divergence of the real part of the dyadic Green's function. As discussed in Section 4 of the main text, this divergence is not included in our calculations concerning the NPoM nanocavity configuration.

References

- 1 M. Kamandar Dezfouli and S. Hughes, *ACS Photonics*, 2017, **4**, 1245–1256.
- 2 H. T. Dung, L. Knoell and D. G. Welsch, *Phys. Rev. A*, 1998, **57**, 3931.
- 3 L. G. Suttorp and A. J. van Wonderen, *EPL*, 2004, **67**, 766–772.
- 4 S. S. Buhmann and S. Yoshi, *arXiv:quant-ph/0006121*.
- 5 M. K. Schmidt, R. Esteban, A. González-Tudela, G. Giedke and J. Aizpurua, *ACS Nano*, 2016, **10**, 6291–6298.
- 6 H. P. Breuer and F. Petruccione, *The Theory of Open Quantum Systems*, Oxford University Press, USA, New York, 2007.
- 7 J. Bechhoefer, *Am. J. Phys.*, 2011, **79**, 1053–1059.
- 8 E. C. Le Ru and P. G. Etchegoin, *Principles of Surface-Enhanced Raman Spectroscopy*, Elsevier, Amsterdam, 2009.
- 9 D. A. Steck, *Quantum and Atom Optics*, available online at <http://steck.us/teaching> (revision 0.13.4, 24 September 2020), 1997.
- 10 M. O. Scully and M. S. Zubairy, *Quantum Optics*, Cambridge University Press, 1997.
- 11 P. Meystre and M. Sargent, *Elements of Quantum Optics*, 2007.
- 12 M. K. Schmidt, R. Esteban, F. Benz, J. J. Baumberg and J. Aizpurua, *Faraday Discuss.*, 2017, **205**, 31–65.
- 13 P. Roelli, C. Galland, N. Piro and T. J. Kippenberg, *Nat. Nanotechnol.*, 2016, **11**, 164–169.
- 14 R. Esteban, J. Aizpurua and G. W. Bryant, *New J. Phys.*, 2014, **16**, 013052.
- 15 Y. Zhang, J. Aizpurua and R. Esteban, *ACS Photonics*, 2020, **7**, 1676–1688.
- 16 M. Paulus, P. Gay-Balmaz and O. J. F. Martin, *Phys. Rev. E*, 2000, **62**, 5797–5807.
- 17 G. W. Ford and W. H. Weber, *Phys. Rep.*, 1984, **113**, 195–287.
- 18 A. Y. Nikitin, F. J. Garcia-Vidal and L. Martin-Moreno, *IEEE J Sel Top Quantum Electron*, 2013, **19**, 4600611.
- 19 M. J. Frisch, G. W. Trucks, H. B. Schlegel, G. E. Scuseria, M. A. Robb, J. R. Cheeseman, G. Scalmani, V. Barone, G. A. Petersson, H. Nakatsuji, X. Li, M. Caricato, A. V. Marenich, J. Bloino, B. G. Janesko, R. Gomperts, B. Mennucci, H. P. Hratchian, J. V. Ortiz, A. F. Izmaylov, J. L. Sonnenberg, D. Williams-Young, F. Ding, F. Lipparini, F. Egidi, J. Goings, B. Peng, A. Petrone, T. Henderson, D. Ranasinghe, V. G. Zakrzewski, J. Gao, N. Rega, G. Zheng, W. Liang, M. Hada, M. Ehara, K. Toyota, R. Fukuda, J. Hasegawa, M. Ishida, T. Nakajima, Y. Honda, O. Kitao, H. Nakai, T. Vreven, K. Throssell, J. A. Montgomery, Jr., J. E. Peralta, F. Ogliaro, M. J. Bearpark, J. J. Heyd, E. N. Brothers, K. N. Kudin, V. N. Staroverov, T. A. Keith, R. Kobayashi, J. Normand, K. Raghavachari, A. P. Rendell, J. C. Burant, S. S. Iyengar, J. Tomasi, M. Cossi, J. M. Millam, M. Klene, C. Adamo, R. Cammi, J. W. Ochterski, R. L. Martin, K. Morokuma, O. Farkas, J. B. Foresman and D. J. Fox, *Gaussian~16 Revision B.01*, 2016, Gaussian Inc. Wallingford CT.
- 20 J. R. Lombardi, R. L. Birke, T. Lu and J. Xu, *J. Chem. Phys.*, 1986, **84**, 4174–4180.
- 21 Y. Fang, Y. Li, H. Xu and M. Sun, *Langmuir*, 2010, **26**, 7737–7746.
- 22 N. Kongsuwan, A. Demetriadou, M. Horton, R. Chikkaraddy, J. J. Baumberg and O. Hess, *ACS Photonics*, 2020, **7**, 463–471.
- 23 F. Benz, M. K. Schmidt, A. Dreismann, R. Chikkaraddy, Y. Zhang, A. Demetriadou, C. Carnegie, H. Ohadi, B. De Nijs, R. Esteban, J. Aizpurua and J. J. Baumberg, *Science*, 2016, **354**, 726–729.
- 24 A. Lombardi, M. K. Schmidt, L. Weller, W. M. Deacon, F. Benz, B. de Nijs, J. Aizpurua and J. J. Baumberg, *Phys. Rev. X*, 2018, **8**, 11016.
- 25 C. M. Galloway, E. C. Le Ru and P. G. Etchegoin, *Phys. Chem. Chem. Phys.*, 2009, **11**, 7372–7380.
- 26 R. Carminati, J. J. Sáenz, J.-J. Greffet and M. Nieto-Vesperinas, *Phys. Rev. A*, 2000, **62**, 012712.
- 27 W. Chen, S. Zhang, M. Kang, W. Liu, Z. Ou, Y. Li, Y. Zhang, Z. Guan and H. Xu, *Light Sci. Appl.*, 2018, **7**, 56.
- 28 W. Zhu and K. B. Crozier, *Nat. Commun.*, 2014, **5**, 5228.
- 29 S. L. Kleinman, B. Sharma, M. G. Blaber, A. I. Henry, N. Valley, R. G. Freeman, M. J. Natan, G. C. Schatz and R. P. Van Duyne, *J. Am. Chem. Soc.*, 2013, **135**, 301–308.
- 30 K.-Q. Lin, J. Yi, J.-H. Zhong, S. Hu, B.-J. Liu, J.-Y. Liu, C. Zong, Z.-C. Lei, X. Wang, J. Aizpurua, R. Esteban and B. Ren, *Nat. Commun.*, 2017, **8**, 14891.